1.0 Introduction

1.1 Purpose and Goals

The objectives of this study were to determine the lateral extent of an acid mine drainage (AMD) contaminated mine pool located at a depth of about 300 feet and to determine areas of groundwater recharge to the mine pool. Acid mine drainage (AMD) is the most important and serious water quality issue in the Appalachian region of the United States (Kleinmann, 1989). The geophysical data analyzed in this thesis were collected by making an airborne electromagnetic and total magnetic field survey and by using different ground-based electromagnetic geophysical techniques. By using these geophysical frequency domain electromagnetic (FDEM) data to map earth resistivities and conductivities, subsurface structure, including variation in groundwater pH, can be determined. Another goal of this survey was to conduct an extensive field test in order to determine the effectiveness of mapping subsurface AMD and drainage paths using combined airborne geophysical techniques that included magnetic, electromagnetic (EM) conductivity and very low frequency (VLF) measurements. Another goal, not presented in this study, relates to the mitigation and reclamation of AMD polluted subsurface regions, for example using these geophysical techniques to map abandoned underground mines containing magnetic grout or determining the effectiveness of mine grout injection. The geophysical data were acquired with a DIGHEM^{vres} multi-coil, mulit-frequency electromagnetic system, supplemented by a high sensitivity Cesium magnetometer, and two-channel VLF receiver.

1.2 Study Location

The study area is located in northeastern Preston County, West Virginia within the Muddy and Roaring Creek watersheds (Figure 1.1). This region is referred to as the T&T mine site. In the simplest representation, with respect to subsurface Acid Mine Drainage (AMD) impacted water systems, the subsurface regions can be thought of as containing three pools of AMD contaminated water. With respect to airborne collected FDEM geophysical data the area of investigation encompasses approximately 917 line-miles flown along 124 East/West traverse lines and two orthogonal tie lines (Fugro, 2000). This survey is located within West Virginia coordinate longitudes (79º 30´ – 79º 45´) W and West Virginia latitudes (39º 30´ –39º 40´) N. A Bell 412 helicopter was employed as the platform for this airborne geophysical survey of the muddy Creek and Roaring Creek area (Figure 1.2).
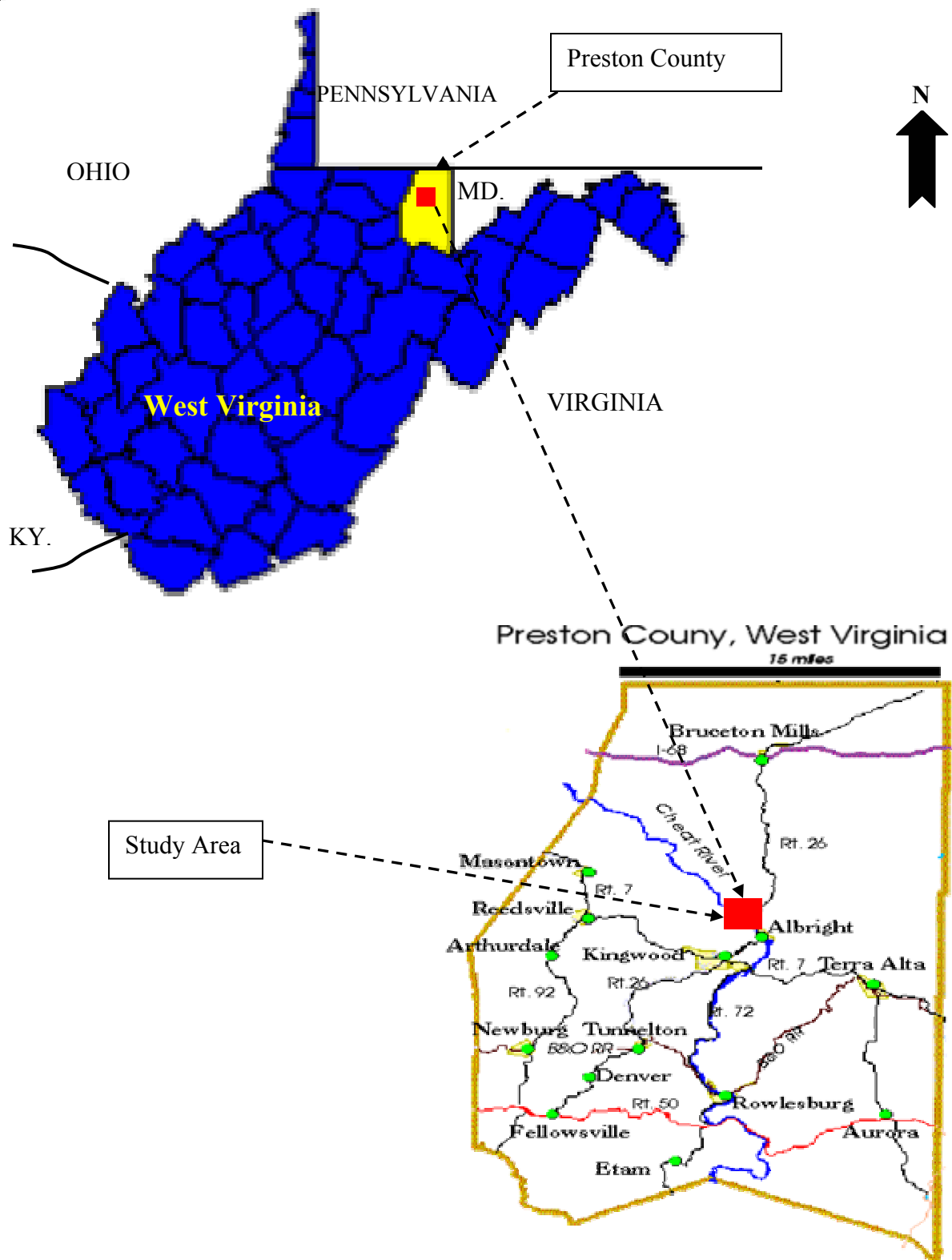
Figure 1.1: The location of study area in Preston County, West Virginia (from West Virginia Geological & Economic Survey URL; http://www.wvgs.wvnet.edu)

Figure 1.2: A Bell 412 helicopter was employed in the Collection of multifrequency conductivity, magnetic, and VLF data. National Energy Technology Laboratory, Department of Energy, URL; http://www.netl.doe.gov).

2.0 Geology and Stratigraphy

2.1 General Geology and Stratigraphy of the study area

The study area is underlain by gradually to moderately folded, consolidated sedimentary rocks of the Allegheny Formation and Conemaugh Group (Hennin and Reger, 1914, and Hobba, 1991). These Middle and Upper Pennsylvanian rocks are comprised mostly of alternating beds of sandstone, shale, and coal that are usually underlain by clay layers. The Upper Freeport coal is about 70 feet below the land surface at the top of the Allegheny Formation (Figure 2.1). In this site, the overburden rock above the Upper Freeport coal is the Conemaugh Group. The maximum thickness of the Conemaugh Group reaches about 640 feet in Preston County (Hobba, 1991).

The stratigraphic column exposed within the study area consists of Pennsylvanian age rock ascending from the Lower Freeport sandstone of the Allegheny Formation through the top sandstone of the Conemaugh Group (Figure 2.1). This column consists of approximately 190 feet of sandstone, shales, clays, limestomes, and coals (Meehan, 1980).
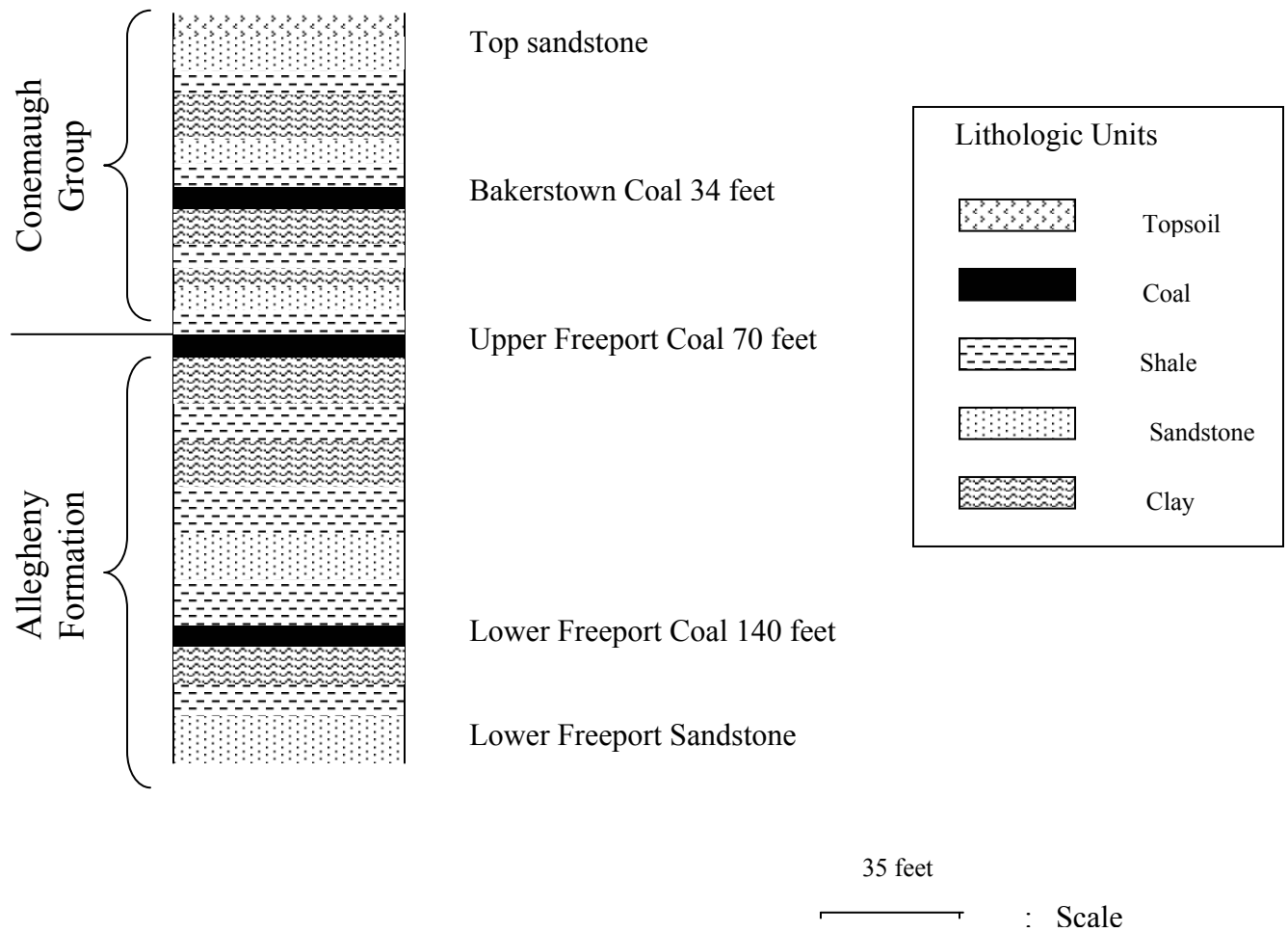
Figure 2.1: Stratigraphic column showing geologic units of the T&T site region (From Hobba, 1991, and Hennen and Reger, 1914).
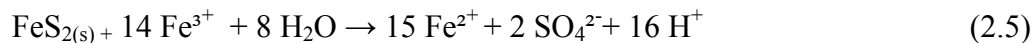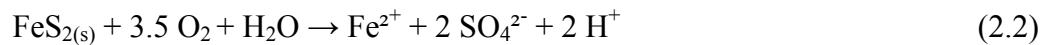
2.2 Acid Mine Drainage (AMD)

Acid mine drainage is the most important and serious water quality problem in the Appalachian region (Kleinmann, 1989). Acid mine drainage is extremely acidic (pH < 2 to 4.5) and rich in iron, sulfate, and heavy metals (Evangelou, 1995). This issue is the oldest and at the same time the most persistent pollution water in the region.

The geochemistry of AMD has been subject of numerous investigations. AMD results from the interaction of certain sulfide minerals with water, oxygen, and bacteria. Pyrite FeS_2 is the most abundant and widely distributed sulfide mineral. The stoichiometry of its oxidation is sometimes written as (Rose and Cravotta, 1998):

$$FeS_{2(s)} + 3.75\ O_2 + 3.5\ H_2O \rightarrow Fe\ (OH)_{3(s)} + 2\ SO_4^{2-} + 4\ H^+ + \text{heat} \qquad (2.1)$$
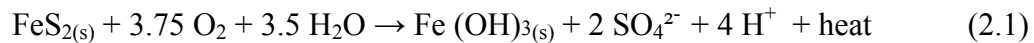
In reaction 2.1, solid pyrite, oxygen, and water are reactants, and solid ferric hydroxide ($Fe\ (OH)_3$), sulfate (SO_4^{2-}), hydrogen ions (H^+), and heat are the reaction products.

The normal reaction may take place in a series of steps:

$$FeS_{2(s)} + 3.5\ O_2 + H_2O \rightarrow Fe^{2+} + 2\ SO_4^{2-} + 2\ H^+ \qquad (2.2)$$

$$Fe^{2+} + 0.25\ O_2 + H^+ \rightarrow Fe^{3+} + 0.5\ H_2O \qquad (2.3)$$

$$Fe^{3+} + 3\ H_2O \rightarrow Fe\ (OH)_{3(s)} + 3\ H^+ \qquad (2.4)$$

$$FeS_{2(s)} + 14\ Fe^{3+} + 8\ H_2O \rightarrow 15\ Fe^{2+} + 2\ SO_4^{2-} + 16\ H^+ \qquad (2.5)$$

In the first step, pyrite reacts with oxygen and water to produce ferrous iron (Fe^{2+}), sulfate (SO_4^{2-}), and hydrogen (2.2). In the second step (2.3), the dissolved ferrous iron is oxidized to form ferric iron (Fe^{3+}). The third step of the reaction (2.4) involves the hydrolysis of ferric iron to form the solid ferric hydroxide (Fe $(OH)_{3(s)}$) and the release of additional hydrogen. In the fourth step, these pyrites oxidized to ferric iron may be reduced by sulfide in a pyrite reaction (2.5). Ferrous iron reenters the cycle in 2.3 as reaction by product. The overall pyrite reaction series is among the most acid producing of all weathering processes in nature (Office of Surface Mining, 2002).

Many factors control the acidity production from AMD including the activity of bacteria, pH, water chemistry, temperature, O_2 concentration, and surface area of the exposed metal sulfide (Stafford, 1999).

Coal mine drainage contains certain amounts of sulfate (SO_4), iron (Fe), manganese (Mn), aluminum (Al), and it also can contain sodium (Na), calcium (Ca), potassium (K), and magnesium (Mg) (Rose and Cravotta, 1998). The precipitation of the iron as hydroxide produce more H^+ and trace metals commonly associated with AMD affect aquatic life, water use, and stream aesthetics. Water polluted by AMD has several characteristics, which make it unusable unless it is treated (Kimmel, 1983).

Therefore, as part of their active and ongoing environmental geophysical program the National Energy Technology Laboratory (NETL) of the U.S. Department of Energy (DOE) collected an airborne geophysical data consisting of five different method FDEM conductivities, total magnetic field, and Very Low Frequency.

3.0 Introduction to Geophysical Instruments and Geology setting

3.1 Electromagnetic Conductivity Methods

3.1.1 Description of the Theory of the Electromagnetic Conductivity Measured

This method estimates the electrical conductivity of the subsurface by using the magnitude and phase of the secondary electromagnetic field produced from an alternating EM (electromagnetic) current source. The primary EM field spreads out in space both above and below the ground and induces electrical currents in subsurface conductors (Figure 3.1), in accordance with the laws of EM induction. These currents give rise to secondary EM fields, which distort the primary field. The resultant field primary + secondary will differ from the primary field in intensity, phase, and direction and can be analyzed to reveal the presence of the conductor (Sharma, 1997).

3.1.1.A. Ground Electromagnetic Conductivity

Most EM, systems employ active transmitters that allow the source geometry and wave frequency to be controlled during the field operations. The main function of the artificial field EM methods is the detection of bodies of high electrical conductivity. Electromagnetic conductivity techniques measure the apparent conductivity of the earth by applying a time varying magnetic field.

Electromagnetic conductivity surveys can be collected on the ground or from aircraft. The primary electromagnetic field travels from the transmitter coil to the receiver coil via paths both above and below the surface. The electrical conductivity in either approach is a function of the electrical properties of the soil and rock matrix, percentage of fluid saturation, and the conductivity of pore fluids. In general, the electrical current flow is

through moist or saturated pore spaces in the soil and rock, not through the mineral grains themselves. Therefore, the bulk conductivity of the geologic units is generally higher than the minerals from which they are composed (Stewart, 1981).
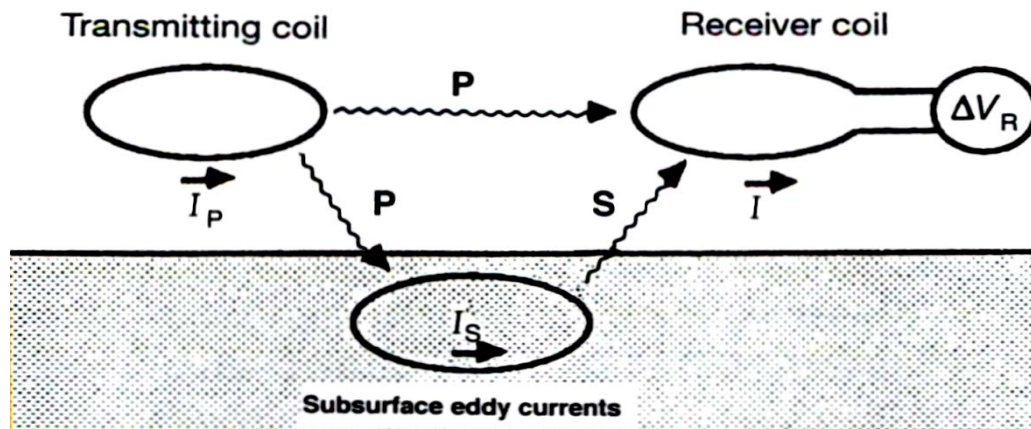

Figure 3.1: A generalized sketch of an electromagnetic induction prospecting system. The transmitting coil, energized with an alternating current (Ip), produces a primary field, which induces eddy currents (Is) in the subsurface conductor. The receiver coil measures the resultant (**R**) of the primary field (**P**) and the secondary field (**S**) induced by subsurface eddy currents (Sharma, 1997).

For this geophysical survey technique, the most favorable targets are metallic ores and underground pipes and cables, although this method has been used in delineating faults, shears, and thin conducting veins. In groundwater studies, targets include groundwater exploration, groundwater mapping, and determining groundwater quality. A major advantage of conductivity methods over the electrical resistivity methods is that they do not require conductive ground connections (Keary et al., 1991).

Four field vectors, described by electromagnetic field theory, are represented by Maxwell's equations (1). Their names, together with their SI units are **E** the electric field intensity (V/m), **H** the magnetizing field intensity (A/m), **B** the magnetic induction, or flux density (Wb/m or tesla), and **D** the electric displacement (c/m) (Sharma, 1997):

$$
\left.
\begin{aligned}
&\text{Curl } \mathbf{E} = -\,\partial\, \mathbf{B}/\partial\, t && \text{(a)}\\
&\text{Curl } \mathbf{H} = \mathbf{J} + \partial\, \mathbf{D}/\partial\, t && \text{(b)}\\
&\text{div } \mathbf{B} = 0 && \text{(c)}\\
&\text{div } \mathbf{D} = \rho c && \text{(d)}
\end{aligned}
\right\}
\qquad (3.1)
$$

In electromagnetic conductivity measurements on the ground (figure 4.2) in the horizontal loop (vertical dipole) currents in the transmitter coil **Tx** produce an alternating current at an audio frequency and in the earth, which is considered as uniform. At a short distance **S** away a receiver coil **Rx** is located. The time- varying magnetic field **Hp** generated by the transmitter coil induces very small currents in the earth. These currents generated a secondary magnetic field **Hs**, which is sensed by the receiver coil together with the primary field **Hp** (McNeill, 1980).

The amplitude of these fields Hp and Hs is a function of frequency, ground conductivity, and other factors.

$$
\frac{\mathbf{Hs}}{\mathbf{Hp}} \cong \frac{i\omega\mu_0 \,\mathbf{s}^2 \sigma}{4}
\qquad (3.2)
$$

Where **Hs** = secondary magnetic field at the receiver coil

Hp = primary magnetic field at the receiver coil

$\omega = 2\pi f$

f = frequency (Hz)

μ_0 = permeability of vacuum

σ = ground conductivity (mho/m)

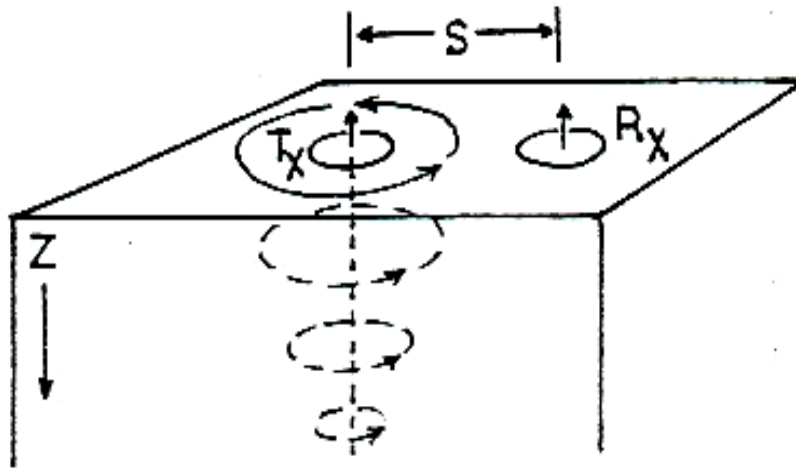s = intercoil spacing (m), and

$i = \sqrt{-1}$.

Figure 3.2: Induced current flow in a homogeneous half-space

Conductivity and resistivity are related by the equation shown below

$$\sigma = 1/\rho \qquad (3.3)$$

Which is σ = ground conductivity (mho/m), and

ρ is the Resistivity (ohm-m)

As shown above, the ratio in the equation (3.2) of the amplitudes of the secondary and primary fields are proportional to ground conductivity. The apparent conductivity can be determined from the ratio these fields using the equation given by McNeill (1980) as

$$\sigma a = \frac{4}{\omega \mu_\circ S^2} \left(\frac{Hs}{Hp} \right) \qquad (3.4)$$

3.1.1.B Airborne Electromagnetic Conductivity

Fugro Geoterrex-Dighem collected the airborne electromagnetic conductivity data using the Dighem ^{VRESI} System. This Multi-frequency electromagnetic conductivity bird used a transmitter and receiver 8 m coil separation, and was towed by a helicopter at approximately 30 m altitude (Figure, 1.2). Five electromagnetic horizontal coplanar frequencies were utilized (380 Hz, 1,400 Hz, 6,200 Hz, 25,000 Hz, and 102,000 Hz).

In order to check the airborne results, EM 34 and EM 47 devices were used. In these devices, the depth of the measurement is a function of the coil spacing, (which is the spacing between transmitter and receiver coil of 10, 20, and 40 meters). These loops can be used in two different modes. Horizontal loops (vertical dipoles) with the effective depth are 1.5, or 15, 30, and 60 meters, vertical loops (horizontal dipoles) with the effective depth are 0.75 S, or 7.5, 15, and 30 meters (Table 3.1).

Intercoil Spacing (Meter)	Approximate Exploration Depth (meter)	
	Horizontal Dipoles	Vertical Dipoles
10	7.5	15
20	15	30
40	30	60

Table 3.1: An example of the depth of measured conductivity for the EM34-3 at various intercoil spacing (From McNeill, 1980)

3.1.2 Description of the Interpretation of the Electromagnetic Conductivity Data

The observed electromagnetic response can be compared with the theoretical response. Theoretical computations of this type are very complex and limited to simple geometric shapes such as spheres, cylinders, thin sheets, and horizontal layers. Master curves are available for simple interpretation of moving source- receiver data where it can be assumed that the conductor has a simple geometric form (Sharma, 1997).

The transmitter frequency and the intercoil spacing determine the depth of penetration. Thus, the differences between conductivity values at different intercoil spacing or frequencies can be used to give some idea of the variation of conductivity with depth (Stewart, 1981). Shallow conductivity anomalies will affect the values at shorter intercoil spacing and higher frequencies. Moreover, the deeper conductivity anomalies will affect the values at longer intercoil spacing and be best-seen using lower frequencies.

Much electromagnetic interpretation is only qualitative, particularly for airborne data. Based on the McNeill equation (3.2), in airborne geophysical survey exploration the depth of measurement increases as the transmitter frequency decreases. For example, in the T&T conductivity dataset, the frequency 380 Hz penetrated to almost 280 feet. The depth of measurement of the frequency 102,000 Hz was only about 17 feet.

3.2 Magnetic Methods

3.2.1. Description of the Theory of the Magnetic Measured

The magnetic method is mostly used in mineral exploration and is widely applied in geo-physical survey from region selection to target identification. The general goal of doing a magnetic survey is to describe the subsurface geology based on the anomalies in the earth's magnetic field caused by lateral or depth variations in the magnetic properties of the underlying rocks

A total intensity vector **T**, uniquely defines the direction and magnitude of the geo-magnetic field at any point on the earth's surface. The magnetic field vector, is described by it's geomagnetic elements (Figure 3.3).
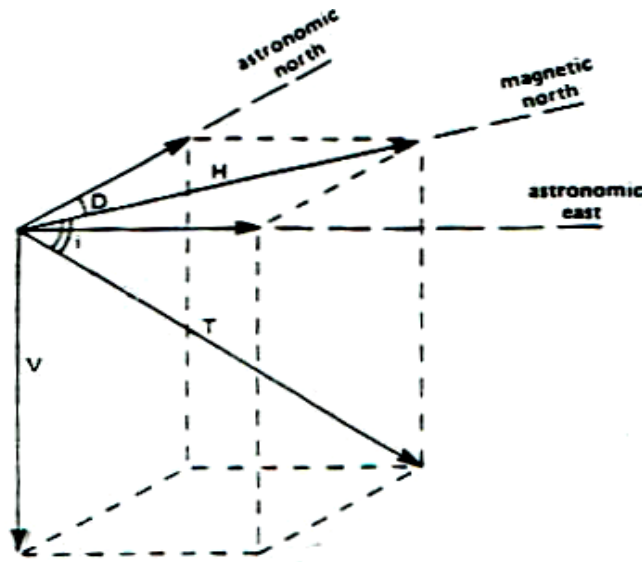

Figure 3.3: Elements of the geomagnetic field (from Gilkeson at el., 1986)

The sides and angles of the parallelepiped shown in the figure 3.3 illustrate the various magnetic elements:

T = total magnetic field vector

V = vertical component vector

H = horizontal component vector

D= angle of declination between the direction of H (magnetic field) and true (astronomic) north

I = angle of inclination of T below the horizontal plane

Magnetic susceptibility is the proportionality constant between H and I. For free space or a vacuum this constant is zero. In the case of a homogenous external field **H** that define an angle θ with respect to the normal to the surface of a material capable of being magnetized, the intensity of magnetization **I** per unit area is (Dobrin at el., 1988):

$$\mathbf{I} = k \, \mathbf{H} \cos \theta \tag{3.5}$$

Or for a field normal to the surface,

$$\mathbf{I} = k \, \mathbf{H} \tag{3.6}$$

The magnetization contrast of the material is primarily the result of induced magnetization (Dobrin et al., 1988).

3.2.2. Description of the Interpretation of the Magnetic Data

The magnetic anomaly of a finite body invariably contains positive and negative elements arising from the dipolar nature of magnetism. The poles of the magnets are negative on the surface of the body where the magnetization vector enters the body and positive where it leaves the body. The magnetic anomaly of a body of regular shape is calculated by determining the pole distribution over the surface of the body from the intensity of magnetization vector and a direction normal to the end face (Sharma, 1997).

The computation and analysis of magnetic depth solutions is the most important component of any high-resolution aeromagnetic survey interpretation. Also important is the direction of magnetization and horizontal location of the source boundaries. Together these determine the shape of anomaly caused by the source body. These methods are usually very complex (Sharma, 1997).

In general, most amplitude variations seen on magnetic anomaly maps results from variation in basement rock type and direction of magnetization, and not from basement topography. There are many methods used to interpret magnetic data. In the detection of structural trends or geological provinces, structures may be indicated by linear magnetic anomalies or alignment of anomalies and the different magnetic terrains have different magnetic signatures (Blakely, 1995).

Detection and analysis of specific anomaly sources for units with uniform susceptibility, k, and uniform polarization, equation (3.7), can relate magnetic potential to gravity potential resulting from a body of similar shape and size, i.e., magnetic potential (and hence magnetic field) can be found from the gravitational potential for the body (sphere, cylinder, polygon, etc.), using Poisson's equation (Blakely, 1995):

$$U_{mag} = \frac{I}{G\rho}\frac{dU_{grav}}{di}$$ (3.7)

where I = magnetization (polarization) = $k\vec{H}$

i = direction of magnetization

ρ = density (used in getting U_{grav})

G = universal gravitation constant

For a detailed study, forward modeling is often useful. Model (3-D or 2.5-D)parameters such as depth size and location of buried bodies, intensity and direction of magnetization or density of each body, are estimated using the results of the background research. The 3-D modeling program is used to automatically refine the model parameters, minimizing the error between the theoretical and observed data. The 2.5-D modeling program can be used to interactively investigate complex modeling situations. The forward modeling procedures help define the basement topography and structure and delineate any intra-sedimentary magnetic features (from Sander Geophysics Limited, http://www.sgl.com/services/interpr.html).

3.3 Very Low Frequency-Electromagnetic Methods (VLF-EM)

3.3.1. Description of the Theory of the VLF-EM Measured

The VLF technique is often used for estimating the locations of subsurface geological conductors (Sharma, 1997). The VLF systems make use of the energy of distant powerful radio transmitters in the 15-25 kHz range. In this project the Cutler U.S.A. and Seattle U.S.A. were used as VLF radio source transmitters. The antenna of VLF transmitters is effectively a long vertical wire carrying an alternating current. The VLF transmitters produce a uniform high frequency electromagnetic field, consisting of a vertical electric field component and horizontal magnetic field component (Keary at el., 1991). The main magnetic field component is horizontal; the line of magnetic field being concentric circles around the antenna mast (Figure 3.4) (Keary at el., 1991). This method can be used for either ground or from airborne geophysical survey (Reynolds, 1997). The VLF anomalies primarily reflect current gathering and measurements are very sensitive to topographic effects.
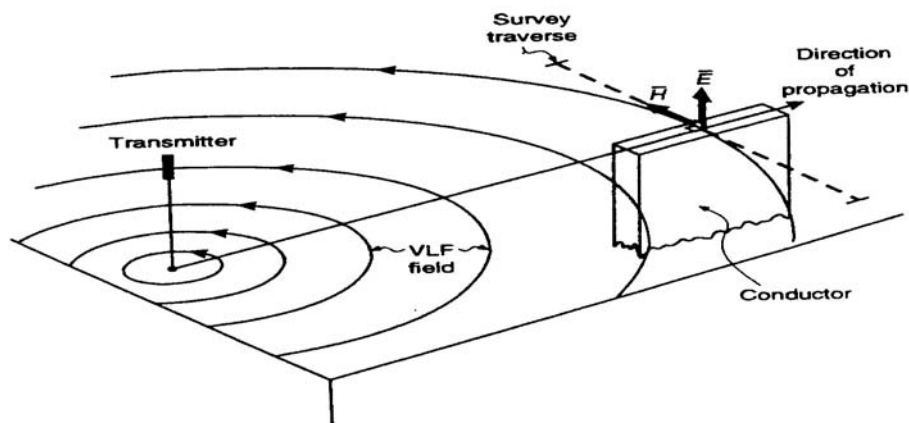

Figure 3.4: Principle of electric and magnetic fields from a VLF radio transmitter. At large distances, the main magnetic field component is horizontal and perpendicular to the direction of propagation and the electric components (Reynolds, 1997).

The VLF survey contained a receiver coil tuned to the frequency of the selected VLF station and a signal detector, and is held with its axis horizontal. Then the coil axis would indicate the bearing of the VLF station (Sharma, 1997). In ground VLF surveys the receiving coil is then turned through 90 degrees, the axis continuing to be horizontal, around its horizontal diameter until a minimum signal is obtained, and the tilt of the coil noted. The tilt gives the angle of inclination of the polarization ellipse. The tangent of the tilt angle provides measure of the ratio of the real component of the vertical secondary field to the horizontal primary field (Figure 3.5) (Sharma, 1997).
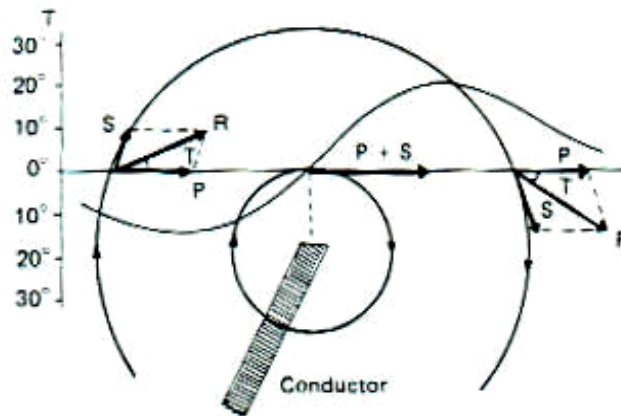
Figure 3.5: Tilt of the electromagnetic field. The primary field is horizontal. R, whose inclination from the horizontal is T, gives the resultant of primary (P) and secondary (S) field (Sharma, 1997).

3.3.2. Description of the Interpretation of the VLF-EM Data

At the present time VLF interpretation is mainly qualitative to date. The characteristics of the measured tilt curve can determine the location of the conductor because it is located directly below the inflection point, where the tilt angle (θ) changes sign. The tilt angle is the inclination from the horizontal. The slope of the tilt curve near the inflection point is a qualitative measure of the depth to the top of the conductor. The asymmetry of the VLF profile gives a rough indication of the dip of the conducting sheet (Sharma, 1997).

Paterson and Ronka (1971) have developed a few rules of thumb that are based on the assumption of a plane, horizontal primary field. These rules relate the horizontal distance between points of maximum and minimum tilt angle to the depth of the conductive body (Figure 3.6). Paterson and Ronka (1971) have given example of the usefulness of VLF surveys in prospecting and geological mapping. Figure 3.6A shows a VLF profile over a mining prospect in Godderham, Ontario, and it's interpretation. Here two or possibly three conductors are indicted. The left-hand anomaly is typical of a good conductor lying close to the surface. The right-hand anomaly is suggestive for a very weak conductor, also close to the surface. The central conductor appears to be an overburden effect. Figure 3.6B shows a VLF profile over a fault zone in the Copper mine River area, Northwest Territories, Canada. The weak, positive response indicates that the fault zone is a poor conductor. Major faults in this area appear to correlate with the stronger, positive VLF anomalies.
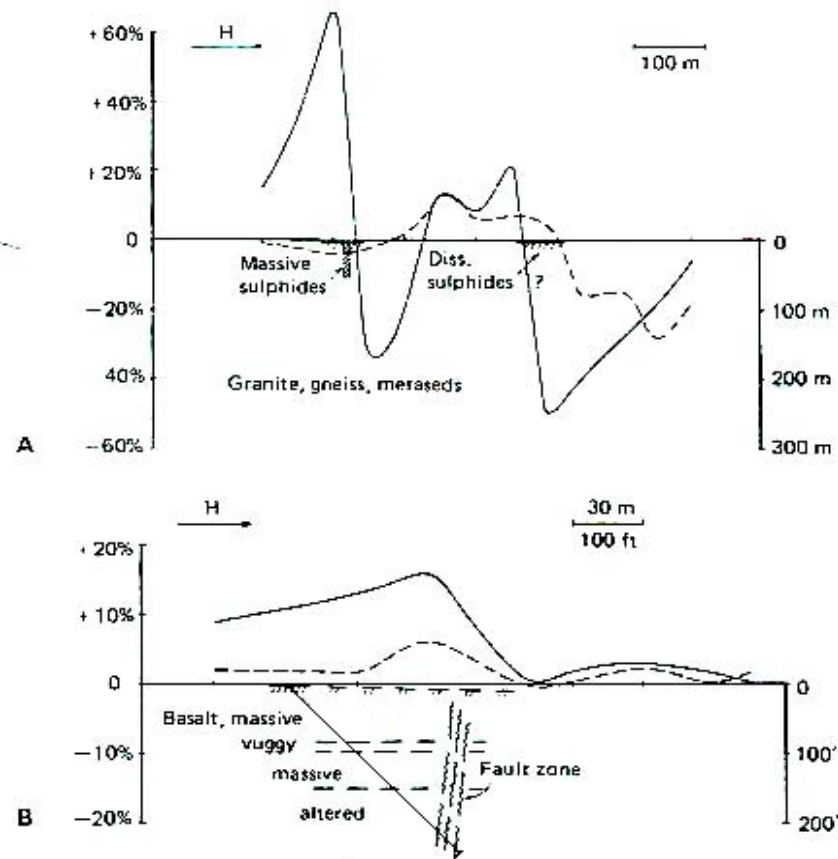
Figure 3.6: Examples of VLF responses over strong and weak conductors. The tangent of measured tilt angle is plotted as the ordinate. (A) VLF profile from the Gooderham mining area, Ontario, indicating locations of three conductors of which one (left) has been confirmed. (B) VLF profile from Copper mine River area, Northwest Territories, Canada, indicating location of the fault zone (From Paterson and Ronka, 1971).

4.0 Data Processing

4.1 Removal of Cultural Electromagnetic Noise from Conductivity Datasets

Noise was the significant issue in the lowest frequency electromagnetic EM conductivity data, especially the 380 Hz and 1400 Hz data. Common cultural interference sources were power lines, pipelines, and vibration of the electromagnetic EM bird. Power lines are the most common source of interference in the northeastern United States. Fortunately, most system noise can be removed through filtering (Valleau, 2000). Therefore, these noise components were removed from the 380 and 1400 Hz. conductivity datasets in Erath Resource Mapper (ER MAPPER) and ERDAS Imagine by applying a variety of spatial frequency filters. ER MAPPER software is geographic and remote sensing image processing software that I used also for geophysical data processing. The important software features are displaying and enhancing raster data, also displaying and editing vector data. This software can link the raster or vector data with Geographic Information System (GIS) data (ER MAPPER, 1998).

The second software packages ERDAS Imagine, incorporates the function of both image processing image analysis and geographic information system (GIS) analysis. In ERDAS software this incorporates include importing, viewing, altering, and analyzing in both raster and vector datasets (ERDAS Imagine, 1997).

4.1.1 High Pass filter in ER MAPPER Software

ER MAPPER was the first technique I used to remove cultural electromagnetic noise from our data. In this method the frequency filtering was used to derive a high-spatial frequency layer that was subtracted from the original data. Briefly, the procedures in this

software were, first view the final raster image after I removed the noise. I then edited the Transform Limits by applying the limits to actual, then set output limits to input limits, and finally created a final linear transform. After that, I used data filtering by editing and identifying different spatial frequencies. For instance, I assumed that the raw data contain both the useful signals and noise, so I used the output from a high pass filter operation to represent the noise. Then I applied a simple formula to create a new image by using the first input of this formula as the original dataset subtracted from the second input that the image was showing the high spatial frequency noise layer. After subtracting the high spatial frequency noise in this manner the overall data quality was significantly improved (Figure 4.1).

The Raw 380 Hz Datasets

The Raw Apperent Conductivity 380 Hz

After using the High frequency filter
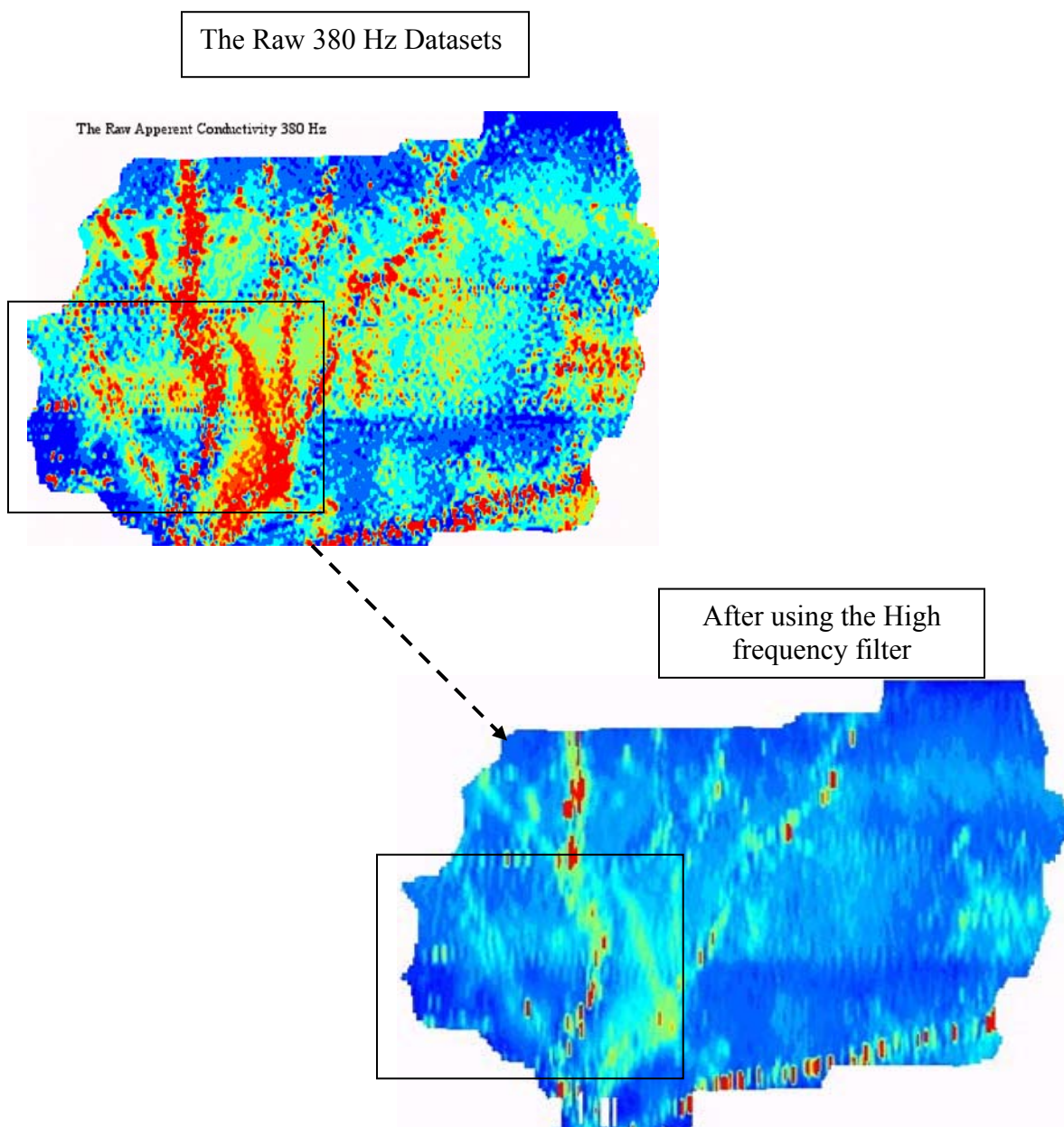
Figure 4.1: An example Frequency 380 Hz that has high culture noise. Two images

showing data before and after ER MAPPER filtering

4.1.2 Homomorphic Filter in ERDAS Imagine Software

In the second method, a Homomorphic filter was applied to the conductivity data to create a dataset consisting of the isolated cultural noise. Homomorphic filtering is a frequency domain filtering process, specifically an image enhancement application that compresses the brightness from lightning conditions, while enhancing the contrast from reflectance properties of the objects (Owens, 1997). Normally images are consisting of light reflected from objects, the portions of light are called the illumination (i) and reflectance (r) components. The functions i and r combine multiplicatively to give the image function F:

$$F(x,y) = i(x,y)r(x,y), \tag{4.1}$$

where $0 < i(x,y) < \infty$ and $0 < r(x,y) < 1$.

When the image formation process is viewed as a product of image illumination and scene reflectance, it is natural to remove the low frequency variations due to illumination by taking the LOG of the image before high pass filtering and then the EXP to display the result (Owens, 1997). This is exactly what Homomorphic filtering does to enhance details in an image. The following diagram (Figure 4.2) summarizes the process of Homomorphic filtering:
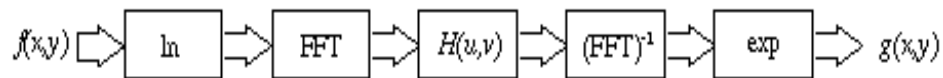
$f(x,y) \Rightarrow \boxed{\text{ln}} \Rightarrow \boxed{\text{FFT}} \Rightarrow \boxed{H(u,v)} \Rightarrow \boxed{(\text{FFT})^{-1}} \Rightarrow \boxed{\text{exp}} \Rightarrow g(x,y)$

Figure 4.2: The process of Homomorphic filtering.

I applied this method by applying the following procedure. First, I imported the data-set in raster format and changed to Grid format. After the images were in Grid format, I started the ERDAS Imagine Software by using Interpreter tools. Fourier analysis was the next step in order to isolate the noise component. I then applied the Homomorphic filter to the raw data. The output of Homomorphic consisted of the high amplitude, high spatial frequency noise component of the data. This isolated noise was then subtracted from the raw data. The resulting dataset was considerably improved.

A simple algorithm was completed as shown in the Figure 4.3 as an example of this process applied to the 380 Hz Conductivity data (Figure 4.4). Below in A) the original 380 Hz Conductivity data is shown. In B) the Homomorphic-extracted noise is shown in map and 3D view (in the 3D view the vertical exaggeration is set to 0.5). In C) the final 380 Hz data, after removal of cultural noise, is shown in map and 3D view (in the 3D view the vertical exaggeration is set to 60).

Represent the
Raw Data Im-
age (380 Hz as
an example)

Represent the
Noise data Im-
age (380_Noise
as an example)

Subtraction
sign
(-)

Represent the
final image after
I removed the
noise from the
Raw data
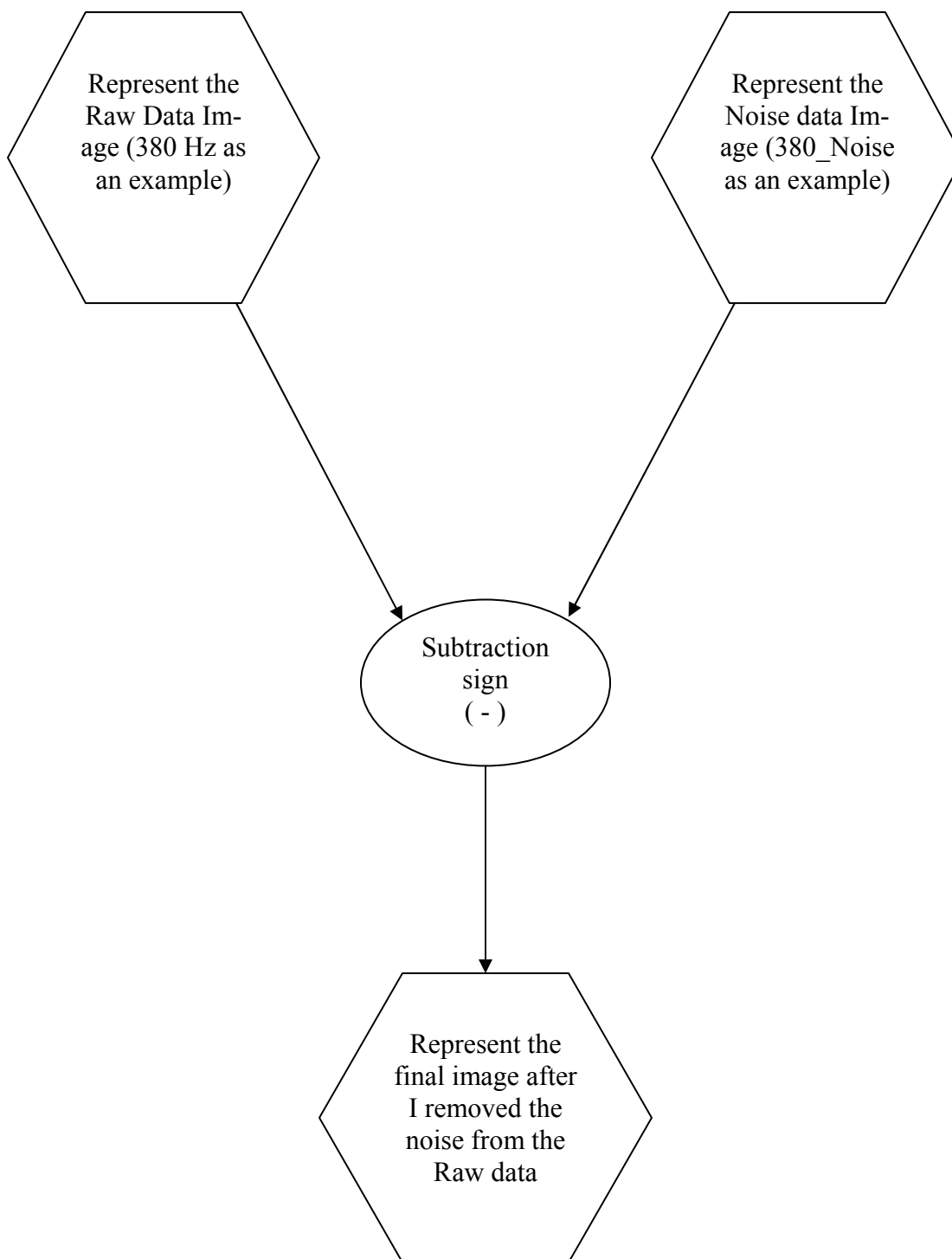
Figure 4.3: An example of the algorithm process I used to remove the noise in ERDAS
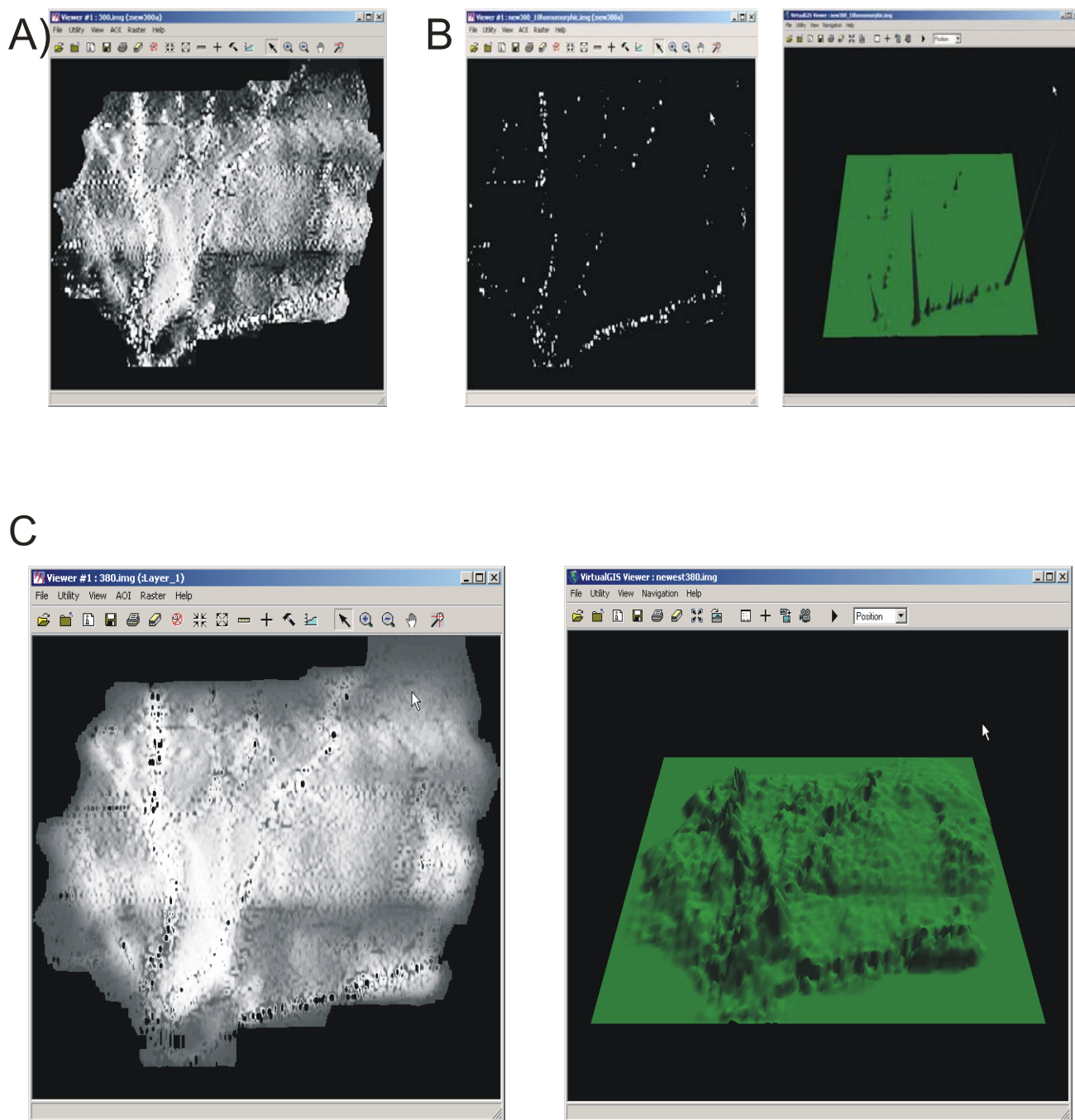Imagine Software

Figure 4.4: An example of Homomorphic filter applied to the conductivity data to create a dataset consisting of the isolated cultural noise.

4.2 Hue Saturation and Intensity (HSI) Algorithm Color Mode

4.2.1 Goal of this technique and the procedures

Hue Saturation and Intensity (HSI) mode is one way of displaying three channels of data. The data in the Hue layer controls the mapping of data values to colors in the spectrum and Hues are what our thinks of as color (red, yellow, green, and so on). The Saturation layer controls the amount of gray in a color purity and the density of the color Low data values or low saturation produce pastel or dull colors (much gray) and high saturation values produce pure or vivid colors (little gray). The third layer, the Intensity layer, controls the mapping of data to the brightness of colors in the image display. High intensity values are bright while low intensity values appear are dark (Figure 4.5)(ER MAPPER, 1998).

False color HSI was a technique I used to determine the geometry of the mine pools area by simultaneously displaying multiple conductivities. I used this technique in ER MAPPER software by creating many different algorithm images substituting the different types of geophysical data in each HSI image and analyzing the HSI images.

The procedures I followed to create the HSI images were:

1. Created one integrated dataset "AllFreq.ers" containing all the geophysical datasets. This dataset consisted of eight layers representing the five Conductivities bands (380 Hz, 1400 Hz, 6200 Hz, 25k Hz and 102k Hz) one total field magnetic and two VLF.

2. Opened a new algorithm image, changed the surface type to HSI and opened three layers one representing the Hue, a second layer representing the Saturation and the third one representing the Intensity.

3. Substituted the types of datasets in each image by choosing a different geophysical datasets in each layer. Thus, I have eight algorithm images and each image represent a different HSI combination of geophysical data.

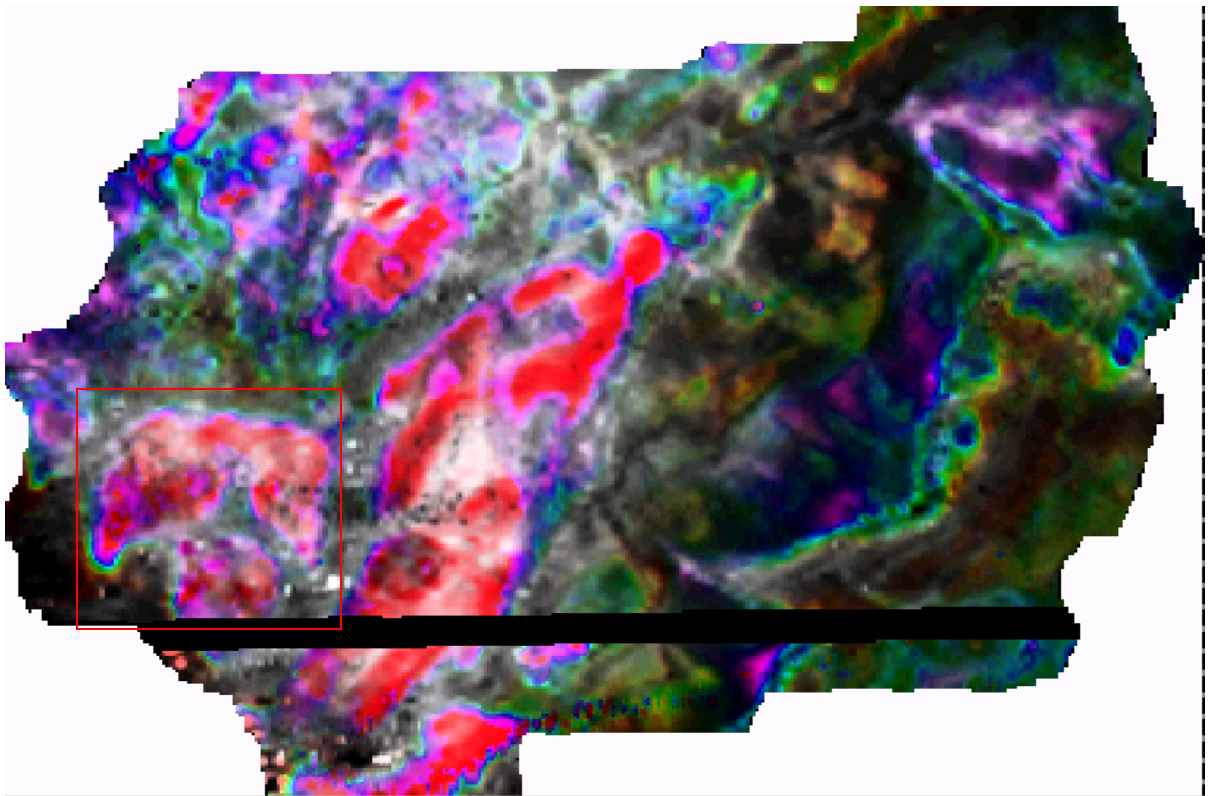4. Opened the transform box and then manipulated the histogram Equalization.

Figure 4.5: An example of the HSI image using 25K Hz frequency as Hue, 1400 Hz

frequency as Saturation, and 6200 Hz as Intensity.

4.3 Unsupervised Classification Technique

4.3.1 Goal of this technique

Classification in general is a process in which all the pixels in an image that have similar spectral signatures are identified (ER MAPPER Software, 1998). Because I wanted to classify the entire image into multiple classes, I chose the unsupervised classification technique. This technique automatically groups all data cells into classes with similar spectral signatures. The goal of application of this method was to determine the geometry of the pools by transforming multispectral image data (all conductivity frequencies, VLF1, VLF2, and total field magnetics) into thematic information classes. I applied this technique using two software packages, ER MAPPER and Arc/Info to create classification images. The reason for using two different software packages for this type of analysis was to compare the results.

4.3.2 Making Unsupervised Classification Images by using ER MAPPER software

Unsupervised Classification is the technique I used to transform multispectral image data into thematic information classes. I used the classification technique as implemented in two different software packages to create classification images. This process was accomplished by first creating the unsupervised classification images in ER MAPPER grouping data cells into a specific number of spectral classes constrained by parameters for when classes were to be split or merged.

The procedures I used to make an unsupervised classification image are first started with creating one raster image that has all the geophysical datasets and put each data in

separate layers. Then statistics were calculated for the dataset. After that, the ISO-CLASS Unsupervised Classification program to cluster the image data into a user-defined number of spectral classes was completed. The next step was specifying the starting classes to start processing, for example in two images (Figure 4.6) I chose ten classes and in the other I chose 255 classes. Displaying the output-classified image and assigning each spectral class a name and color corresponding to a thematic class was the last step.

In the T&T mine area the 255 class ISOCLASS image appeared to accurately outline a mine pool. This mine pool (mine pool A) will be discussed in more detail in a following section of this thesis. The 10 class image did not accurately define mine pool regions.
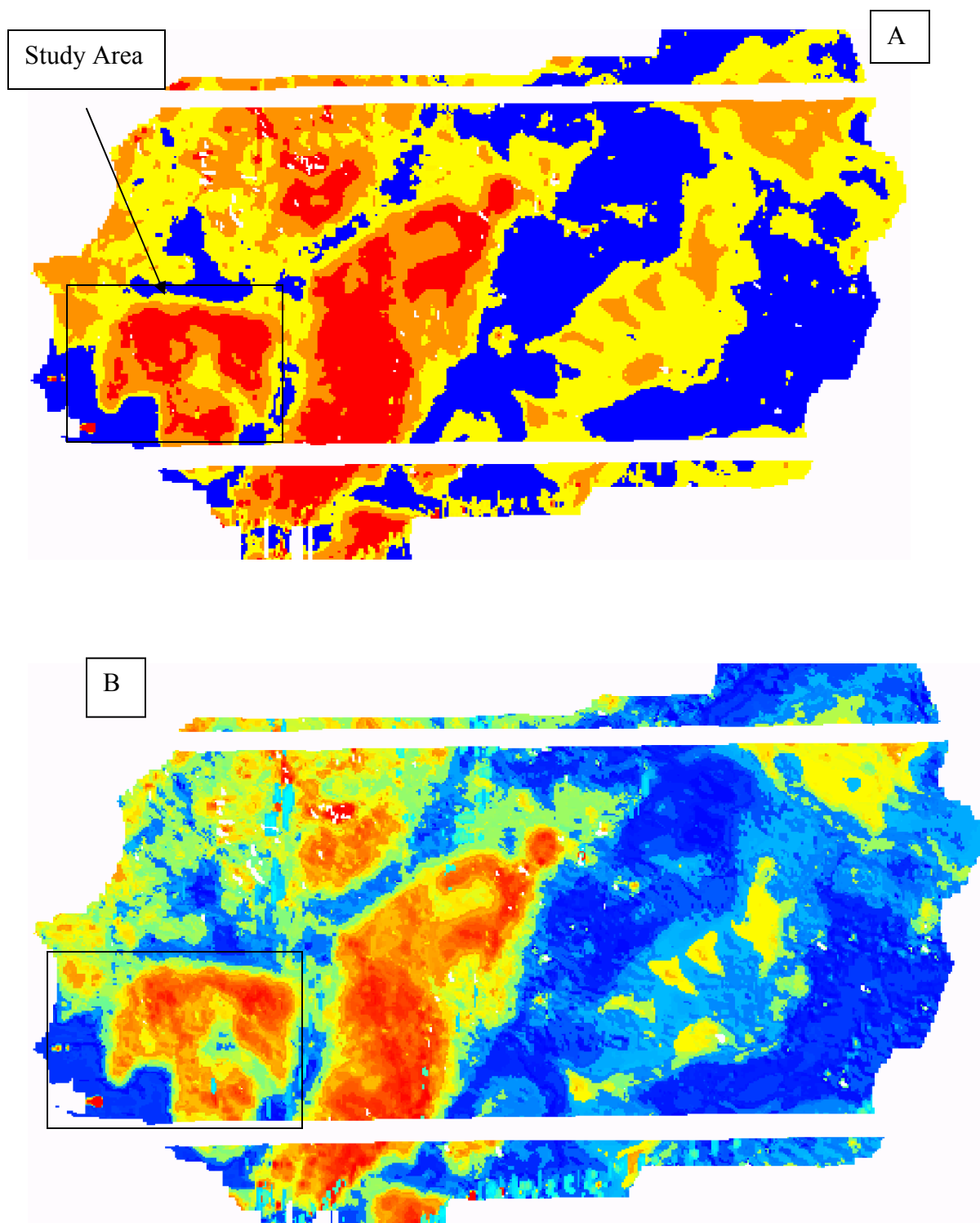
Figure 4.6: Examples of the unsupervised classification images using ER MAPPER software. A) Final ten specifying classes unsupervised classification image. B) Final 255 class ISOCLASS unsupervised classifications.

4.3.3 Making Unsupervised Classification Images by using Arc/ Info

Another method used to create unsupervised classification images is by using the Arc/info software package on UNIX based computer system (Figure 4.7). Before starting converted all the geophysical datasets and DEM data to Arc Grid format using ERDAS Imagine software by following these procedures:

1. Clicking on the Data properties then Reproject Images (because I needed to change the projection of all the datasets from Unknown to projection UTM and Zone 17).

2. Converting the datasets to grid format by using Import → Export box and changing the type file to Grid.

3. After I have all the data on a Grid format, I changed or corrected some of minimum values of each grid, using the Arc/Info command " con".

Here is an example using dataset, (102 Hz) in which I created a new grid and named it New_102grd:

$$Grid: New\_102grd = Con (Grid\_102 \ GE \ -4000, \ Grid\_102)$$

I did the same thing to all the grid datasets.

In the last step, all the grids were used to calculate the statistics for each grid and then create final Classification (ISOCLASS methodology) images in Arc/Info.

In general, the Arc/Info technique does not achieve the main goal clearly when compared with the results from ER MAPPER.
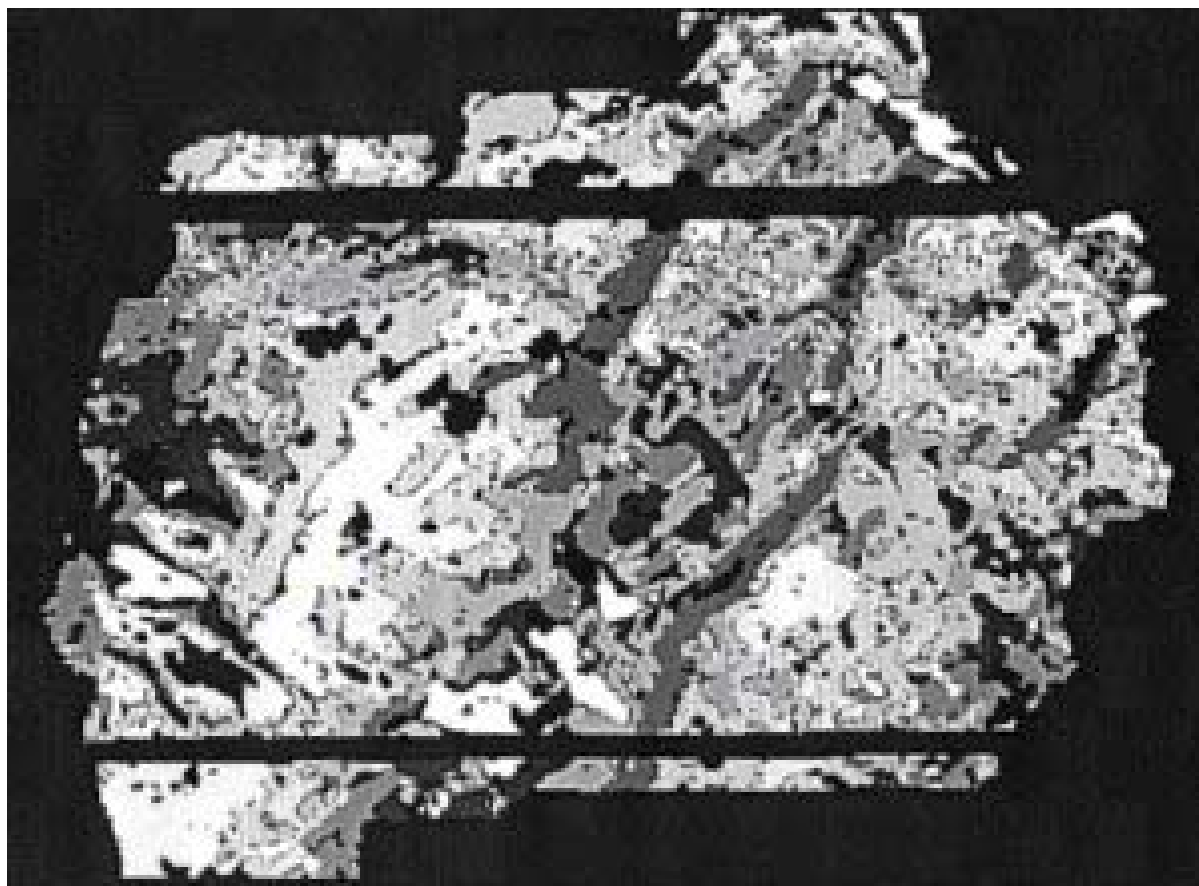
Figure 4.7: Unsupervised classification image calculated using Arc/Info

4.4 Extract cross sections of multifrequency conductivity from the AMD Impacted mine pools area

4.4.1 Goal of this technique and procedures

In this method, a data cube of all conductivity measurements was created. Then the amplitude of the selected bands along a cross section of terrain of the mine pools area was extracted. A series of geophysical cross sections were created in ERDAS Imagine by stacking the conductivity data from highest to lowest frequency along profiles over the mine pools and their edges. In addition, line graphs of conductivity were created for interpretation. Figure (4.8) shows the location map and profiles extracted from this study area.
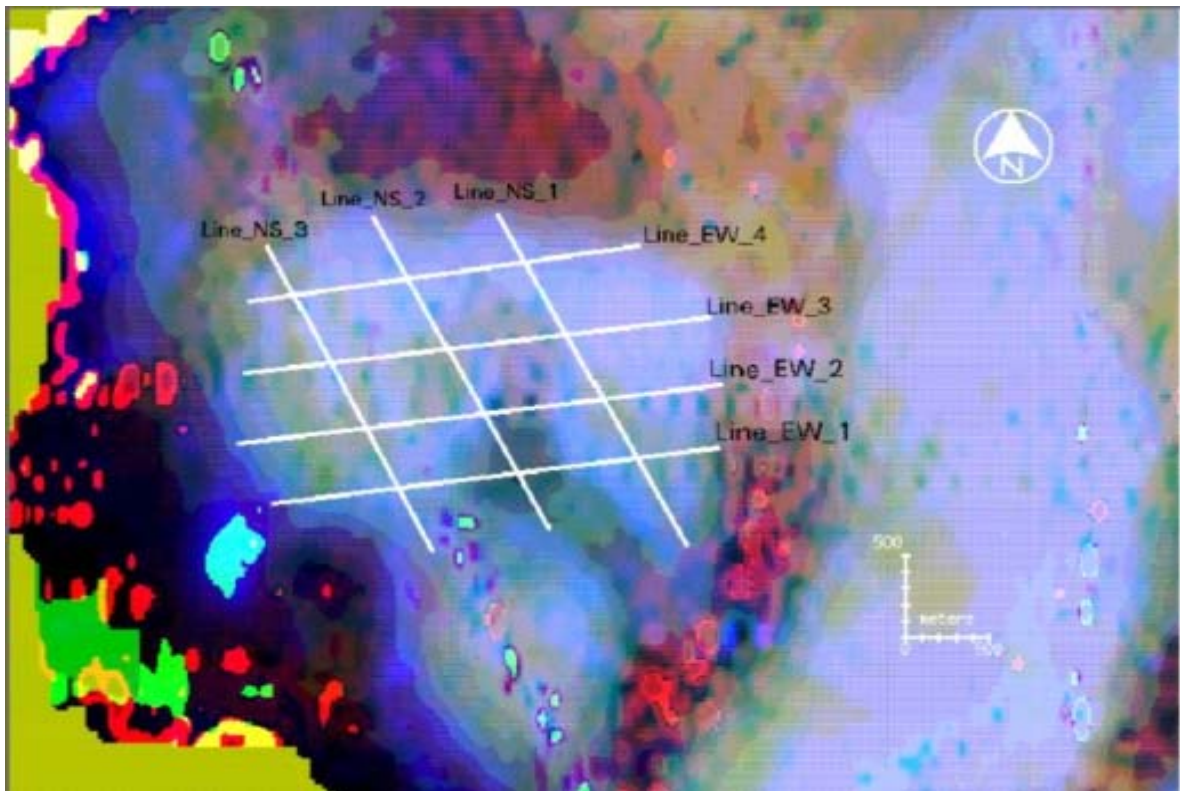
Figure 4.8: The location of extracted geophysical cross sections FDEM conductivity over the mine pools and their edges.

4.4.2 The cross section profiles and they are prospective

This technique helped me to estimate and determine the areas that have high conductivity anomalies. In the T&T site, I divided the coal mine area into three regions, each with a suspected mine pool. These are mine pool-A in the top right side, second in the top left side is mine pool-B, and third part in the mid-bottom in our study area is the mine pool-C region (Figure 4.9).

I then estimated the major anomalies by extracting a 3-D surface profiles from each mine pool region.
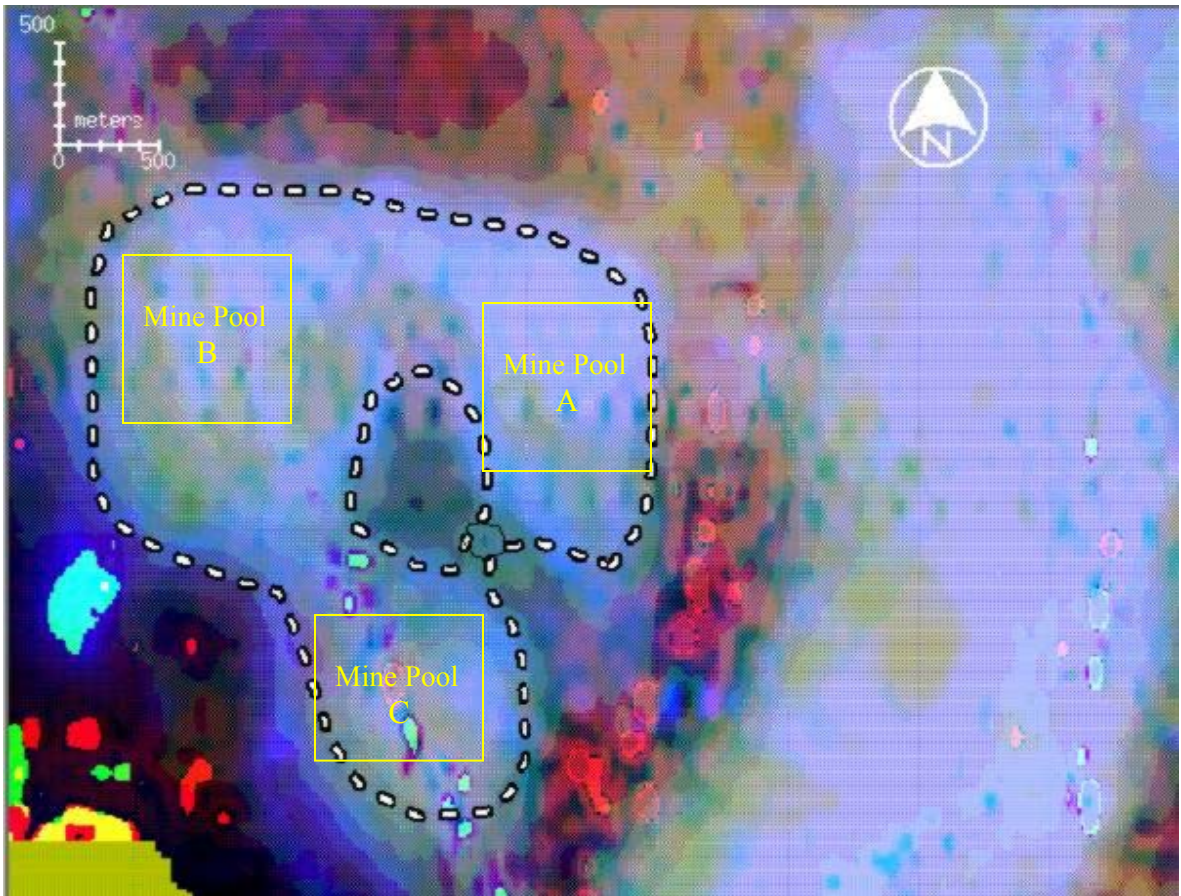
Figure 4.9: The three AMD pool regions in our study area.

There are two high conductivity regions in the 380 Hz and 1400 Hz data in the first line (Line_EW_1) in the figure (4.8). The cross section and the conductivity profile show these high values very clearly in Figure (4.10)
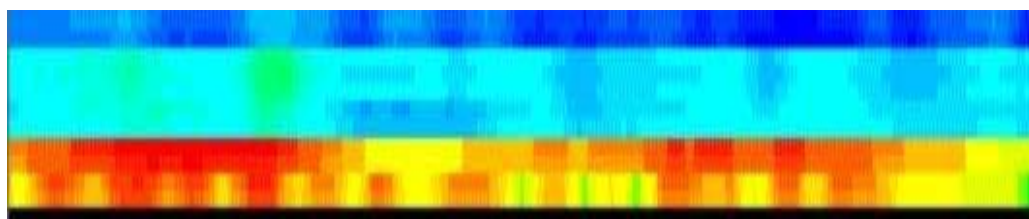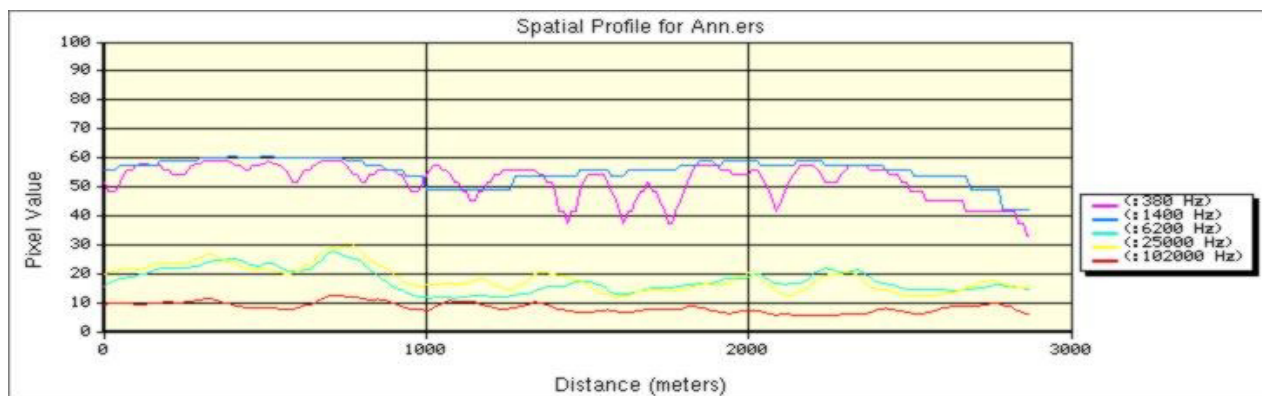
High Conductivity Values
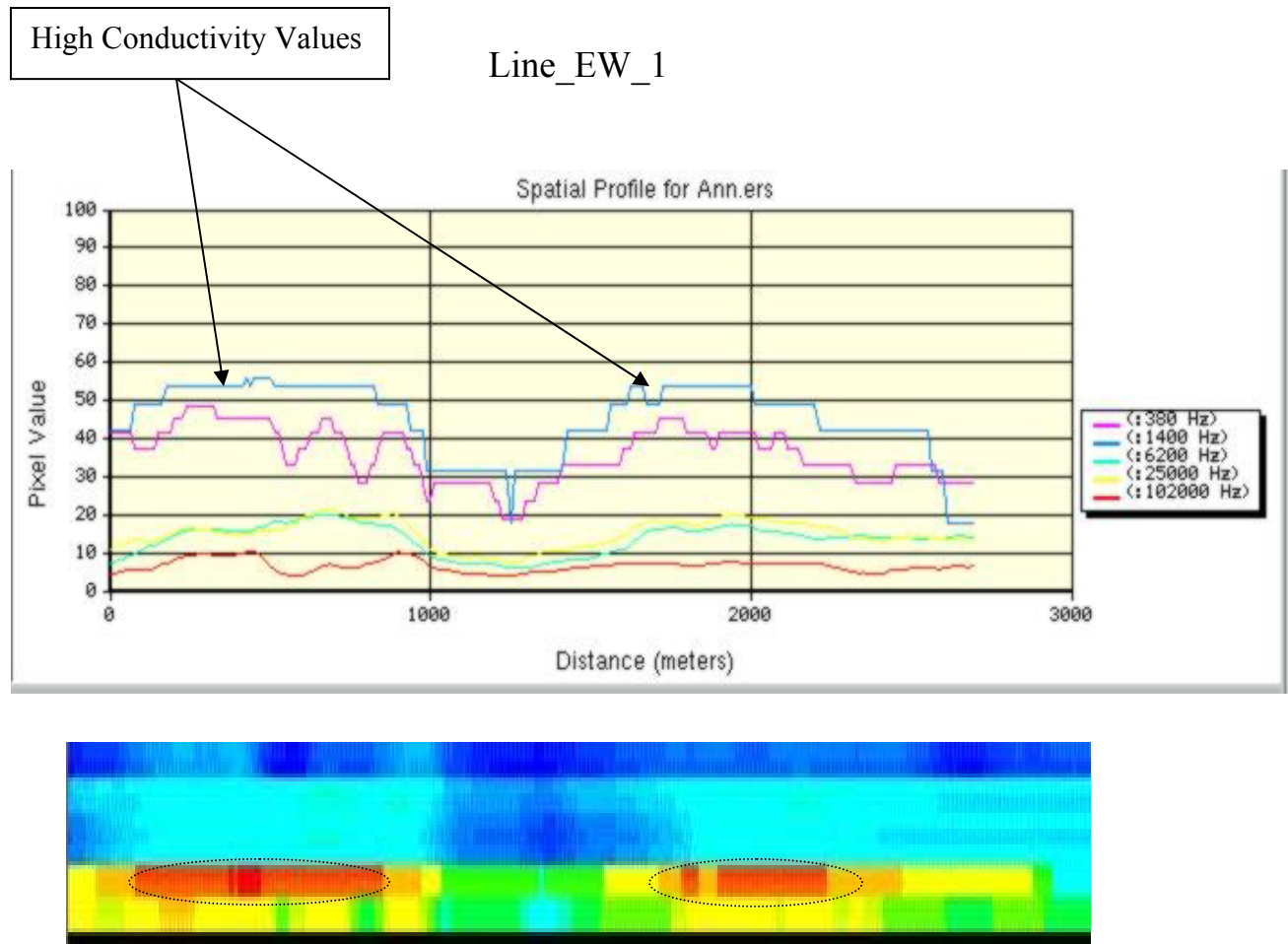
Line_EW_1

Figure 4.10: Profile (Line_EW_1) shows two high-conductivity anomalies surrounding a centrally located low conductivity anomaly.

Both lines "Line_EW_3 and Line_EW_4" in figure (4, 11) show almost similar conductivity values across the mine pools A and B. The middle of Line_EW_4 shows a higher conductivity when compared with the adjacent spot on Line_EW_3. Our interpretation is that this variation is a proxy for the boundary of a high conductivity AMD pool, which I interpret as mine pool A and mine pool B.
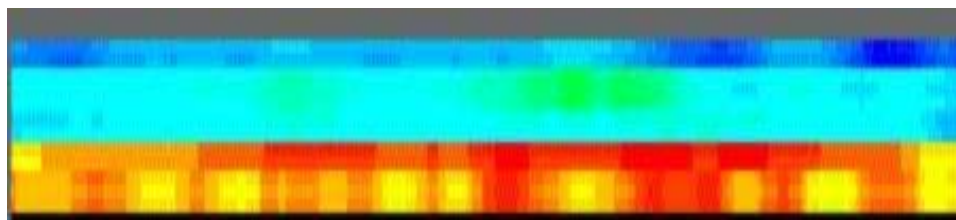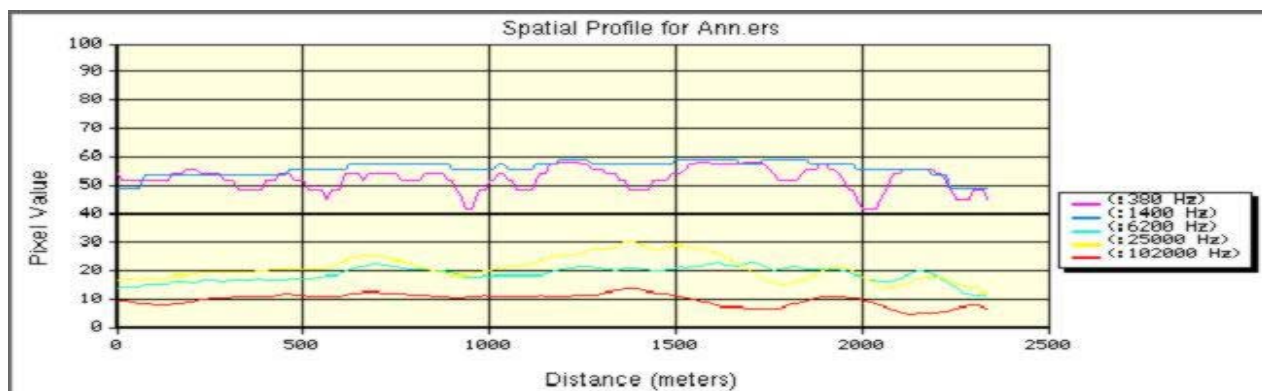
Line_EW_3

Line _EW_4

Figure 4.11: Profiles (Line_EW_3) and (Line_EW_4) show conductivity values across

the mine pools.

Both of these profiles are similar with respect to conductivity. They are located along the western (Line_NS_3) (figure 4.13) and eastern (Line NS_1) (figure 4.12) portions of the study region. These two lines support the model of two mine pools (A and B). Note that the conductivity values at the beginning of each line have nearly the largest values and by moving towards the south, the conductivity values decrease. I interpret these higher values of 380 Hz and 1400 Hz derived conductivity to represent geophysical proxies for the location of mine pools A and B.
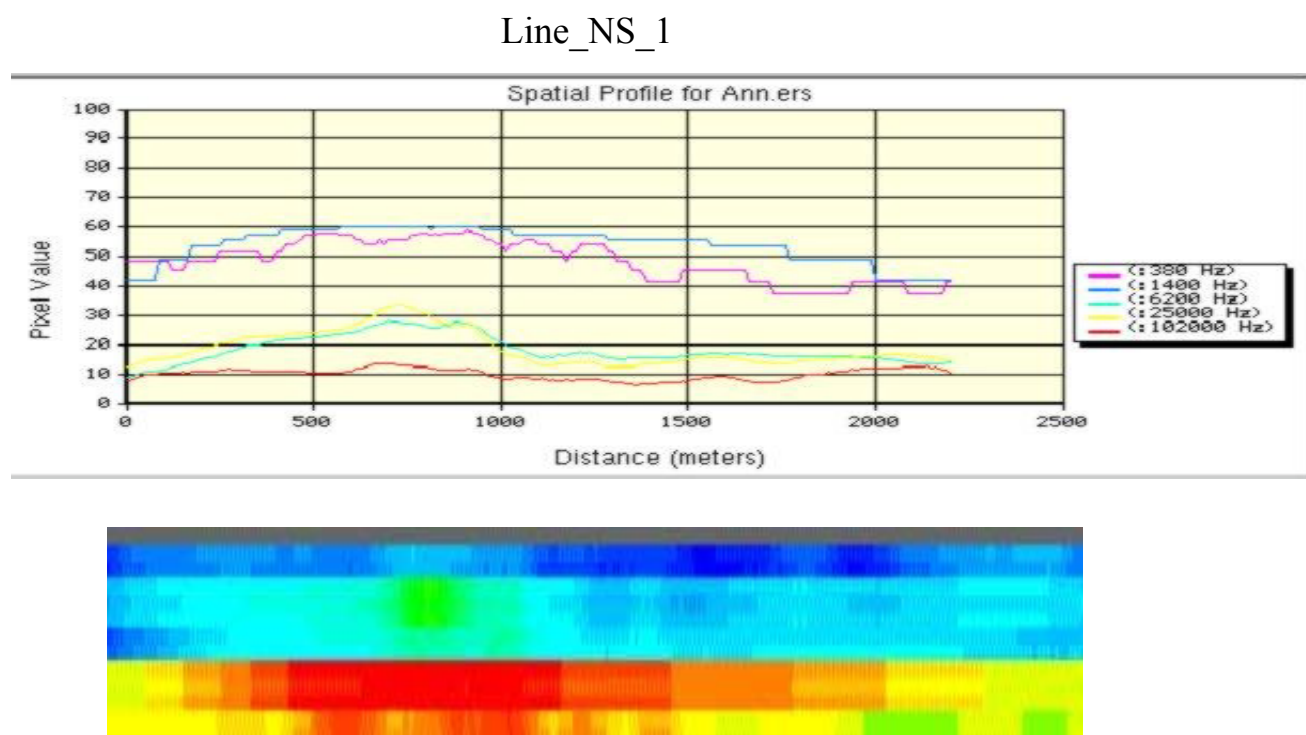
Line_NS_1

Figure 4.12: A profile (Line_NS_1) displaying the conductivity values over the east side
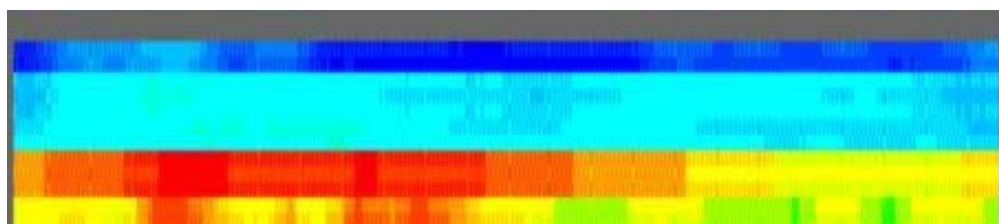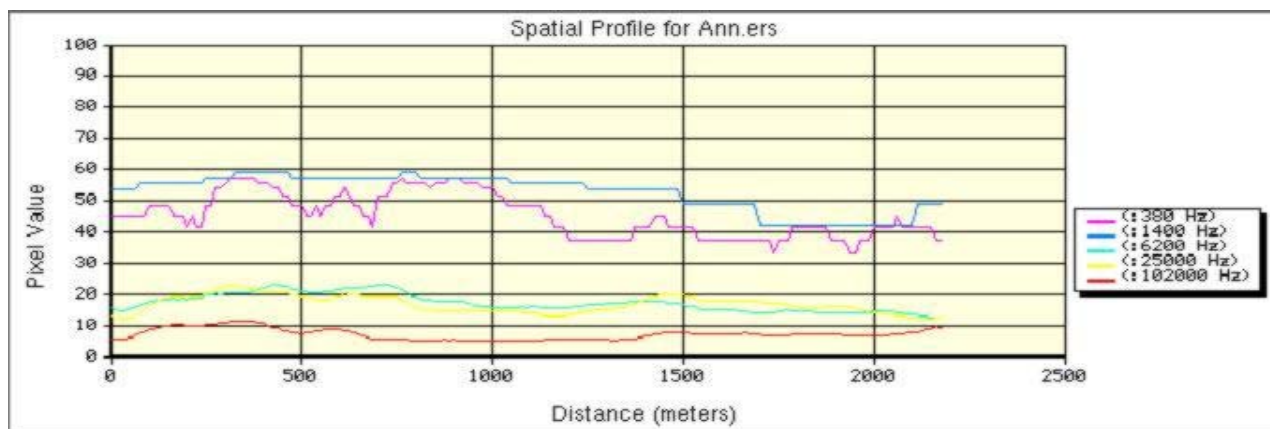
of the mine pools.

Line_NS_3

Figure 4.13: A Profile (Line_NS_3) displaying the conductivity values over the west side

of the mine pools.

Line_NS_2 (figure 4.14) shows the AMD impacted region on the left-hand side of this cross section. Note the rapid decrease in conductivity values in the central portion of Line_NS_2, moving away from the AMD impacted region. I interpret this to represent the geophysical conductivity signature of the boundary of a mine pool.
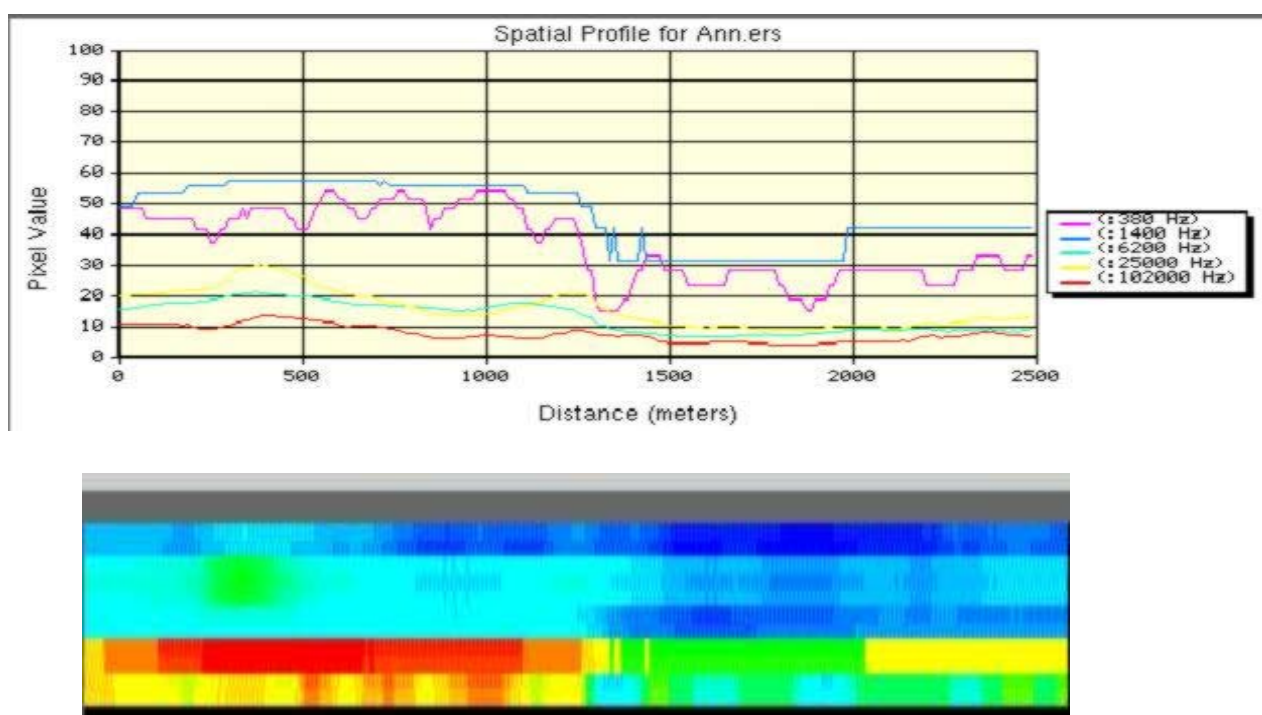
Line_NS_2

Figure 4.14: A profile (Line_NS_2) displaying the conductivity values over the mine

pools.

5.0 Data Interpretations

5.1 Final Results for the Electromagnetic Conductivity.

Figure 5.1 shows a Red/Green/Blue color composite image using RED-380 Hz, GREEN-1400 Hz, and BLUE 25,000 Hz conductivity (using the noise reduced 380 and 1400 Hz data layers). Although cultural noise is still present in the 380 Hz and 1400 Hz conductivity datasets, regions of both high Red and high Green superimposed color components may represent AMD pool regions (Figure 5.1).
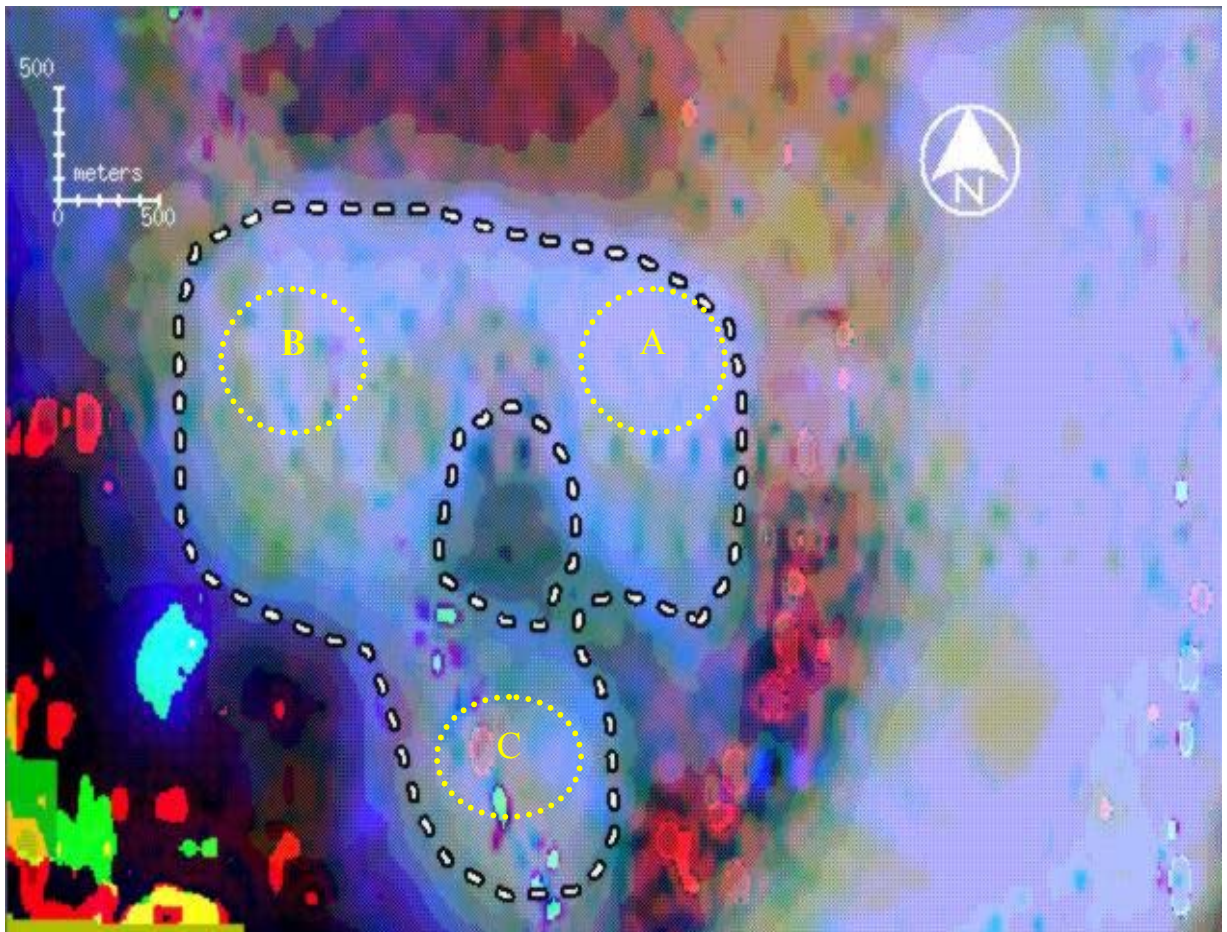

Figure 5.1: A general location map showing the mine pools A, B, and C.

In this portion of the analysis, 3-D surface profiles of all the conductivity datasets (380, 1400, 6200, 25000, and 102000 Hz) were created for the mine pool A region. These conductivities show the largest anomaly in the mine pool A.

Figure (5.2) which shows the 3-D surface profile of the largest frequency 102,000 Hz and the coal mine boundaries profile in mine pool A.
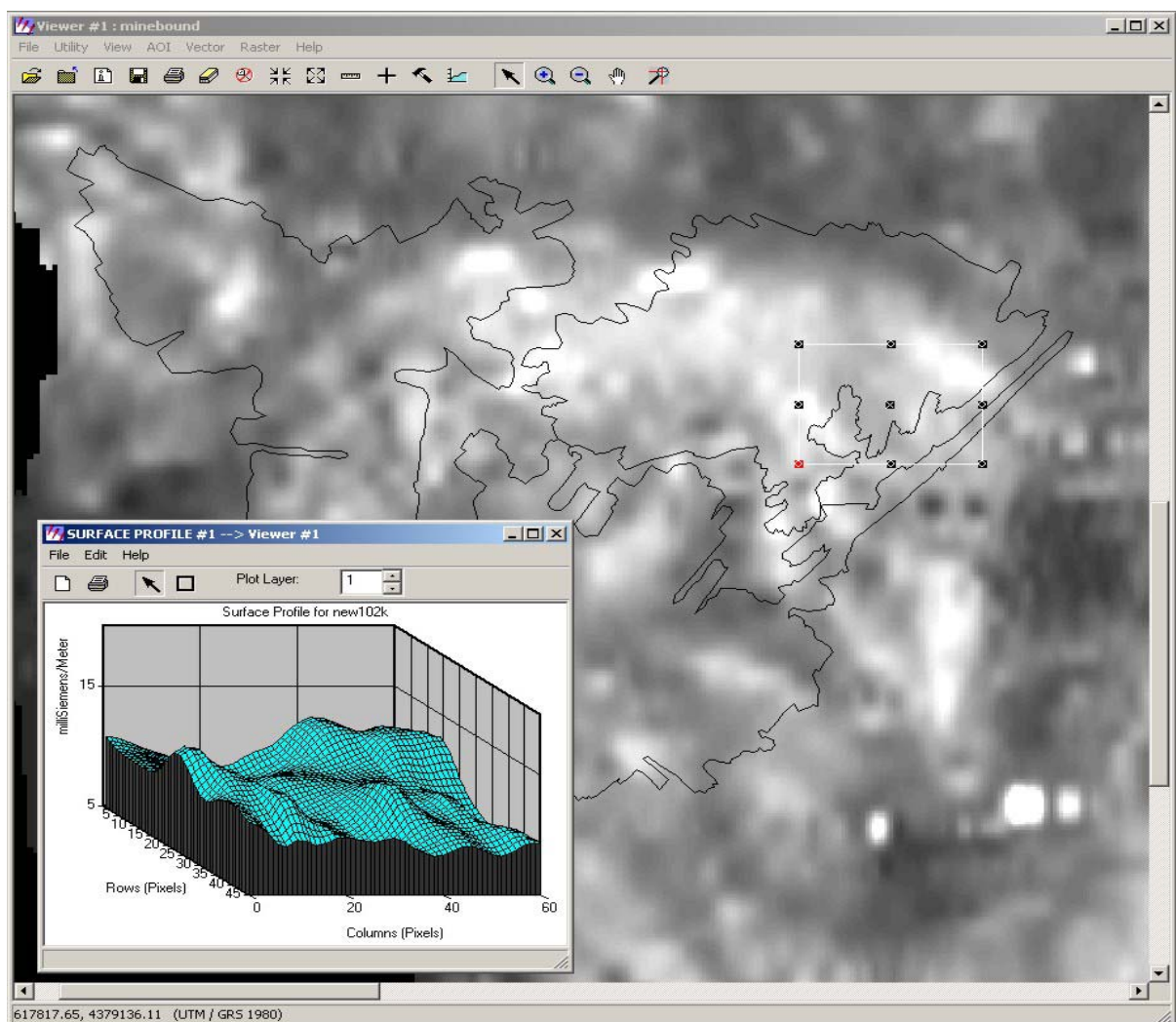

Figure 5.2: The mine boundary of the coal mine area for the 102,000 Hz frequency

.

The conductivity value in the 102,000 Hz frequency does not show any high anomaly (in the data range of values between (7-12) milliSiemens/Meter) and at the penetration depth about 17 feet. By penetrating down with 25,000 Hz frequency, the conductivity values increased and showed conductivity values up to 25 milliSiemens/Meter at a depth about 35 feet (Figure 5.3).
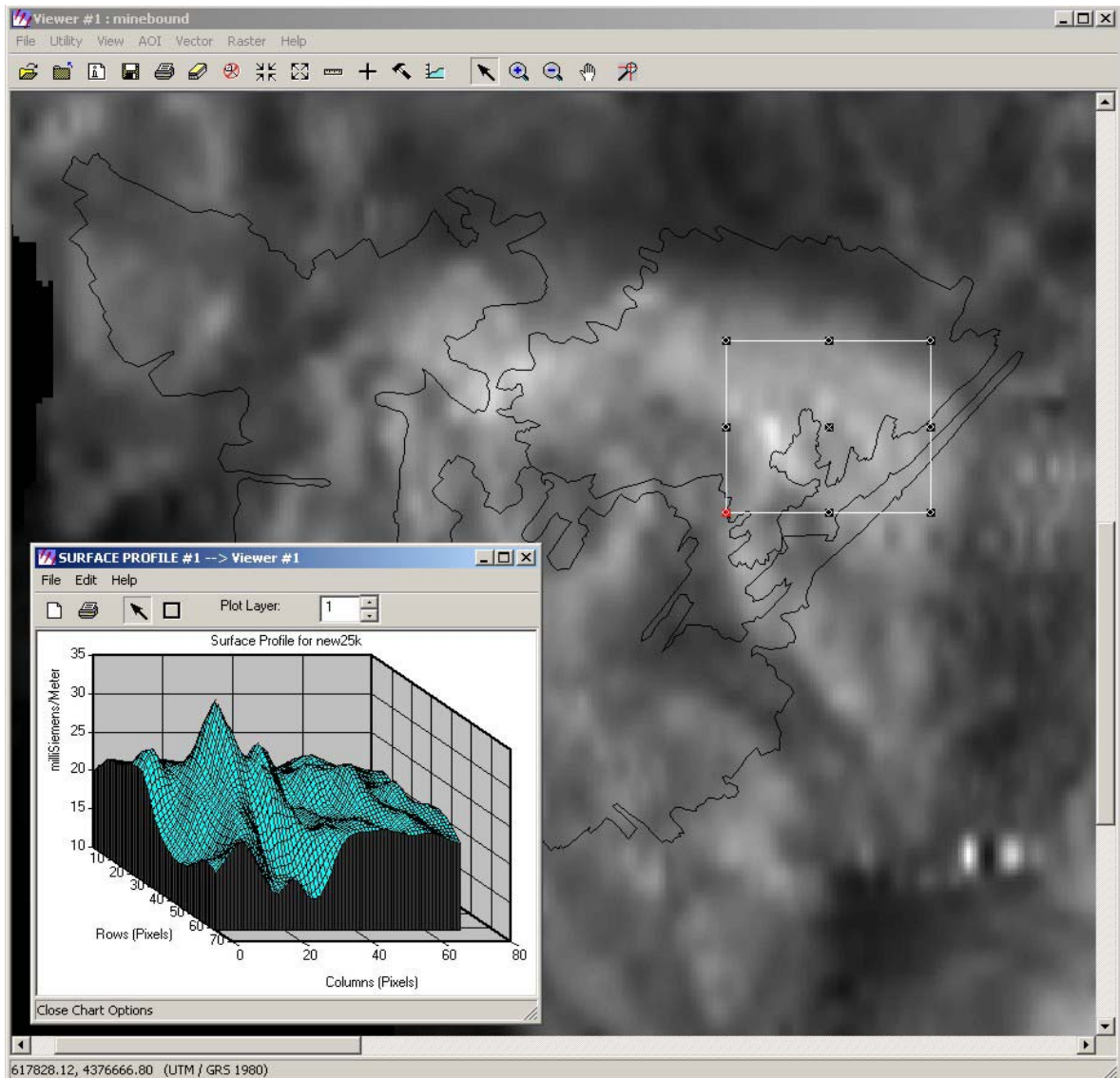

Figure 5.3: The mine boundary of the coal mine area for the 25,000 Hz   frequency

The 6200 Hz frequency image shows an increasing in the conductivity values approximately up to 27 milliSiemens/meter at an approximate depth of 70 feet (Figure 5.4).
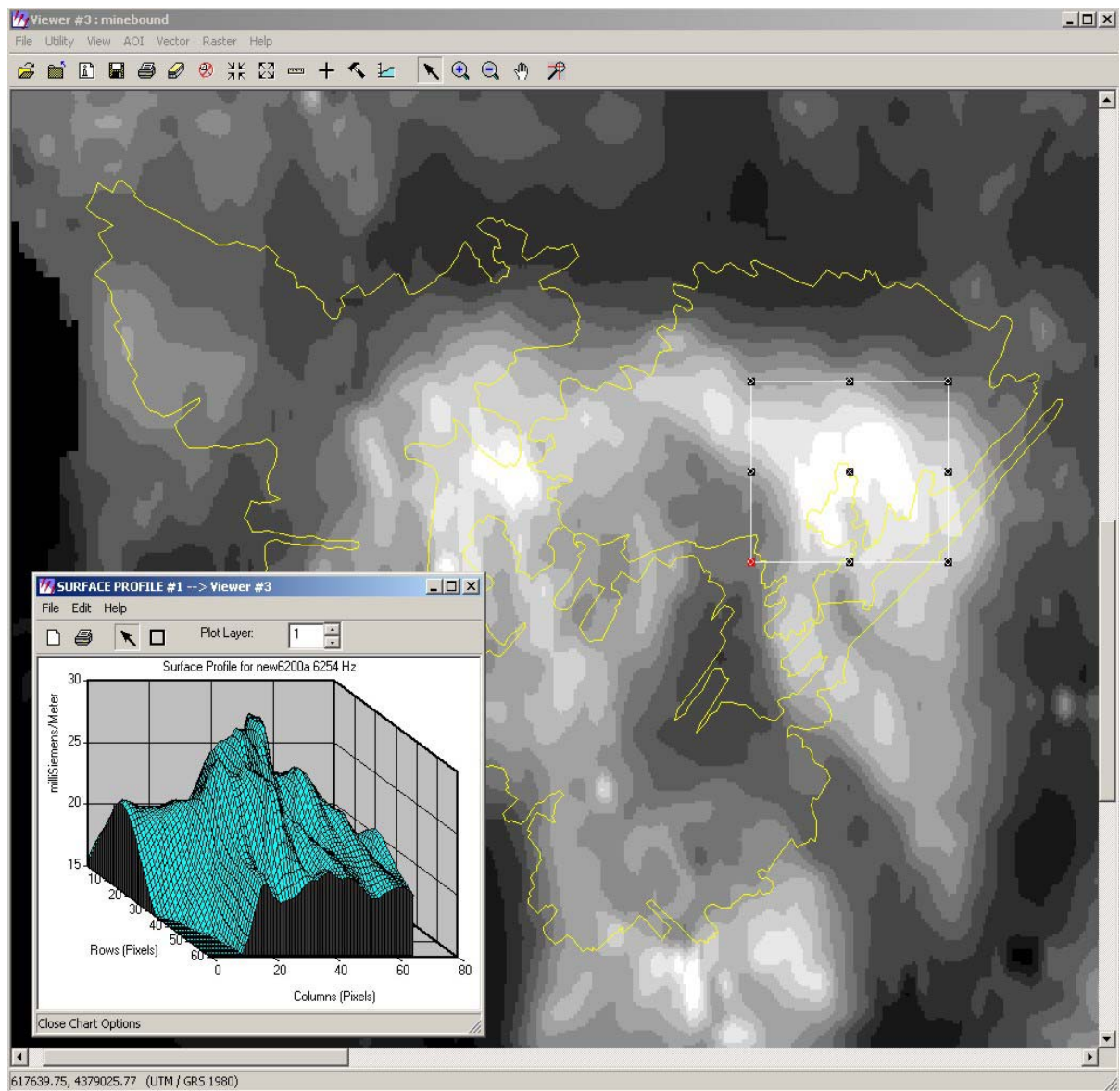
Figure 5.4: The mine boundary of the coal mine area for the 6200 Hz frequency

.

The conductivity values at depths of around 140 feet decreased again, which is represented by the frequency 1400 Hz. These values have good correlation between the airborne data and the conductivity measurements obtained from induction logging of wells in the T&T region. The conductivity values ranged are between 15 to 20 milliSiemens/Meter (Figure 5.5).
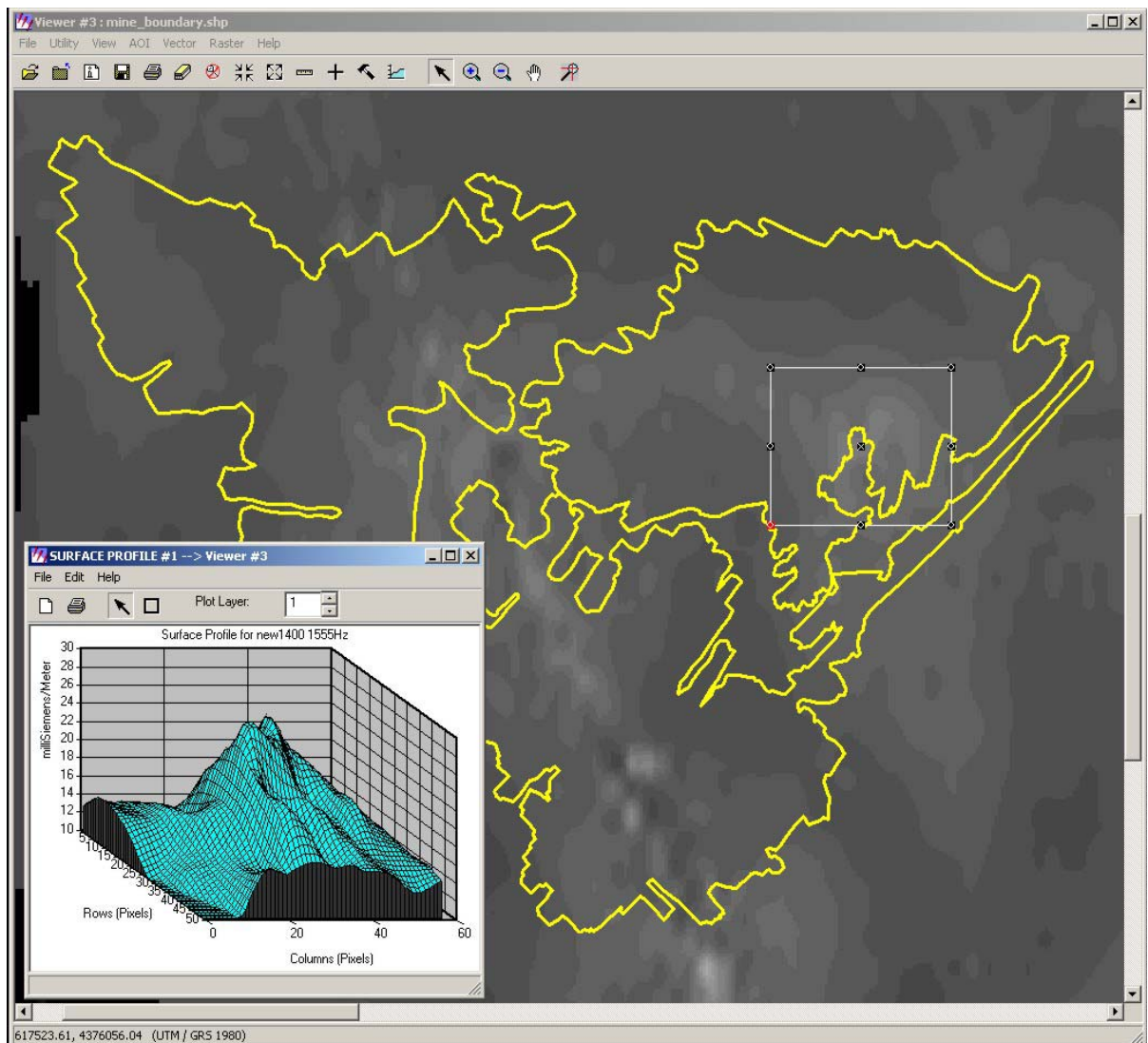

Figure 5.5: The mine boundary of the coal mine area for the 1400 H frequency

In the deepest penetrating and complex frequency, the 380 Hz, high conductivity and a very high anomaly is seen in the mine pool A region at approximately 280 feet depth. The 380 Hz frequency is the most sensitive to power lines interference (Fugro, 2000). Therefore, in the Fugro calculation the 380 Hz has not been used when an area contains power lines (Figure 5.6). However, because of the removal of noise from the 380 Hz data, discussed earlier in this thesis I have considered in my interpretation the lowest frequency conductivity data.
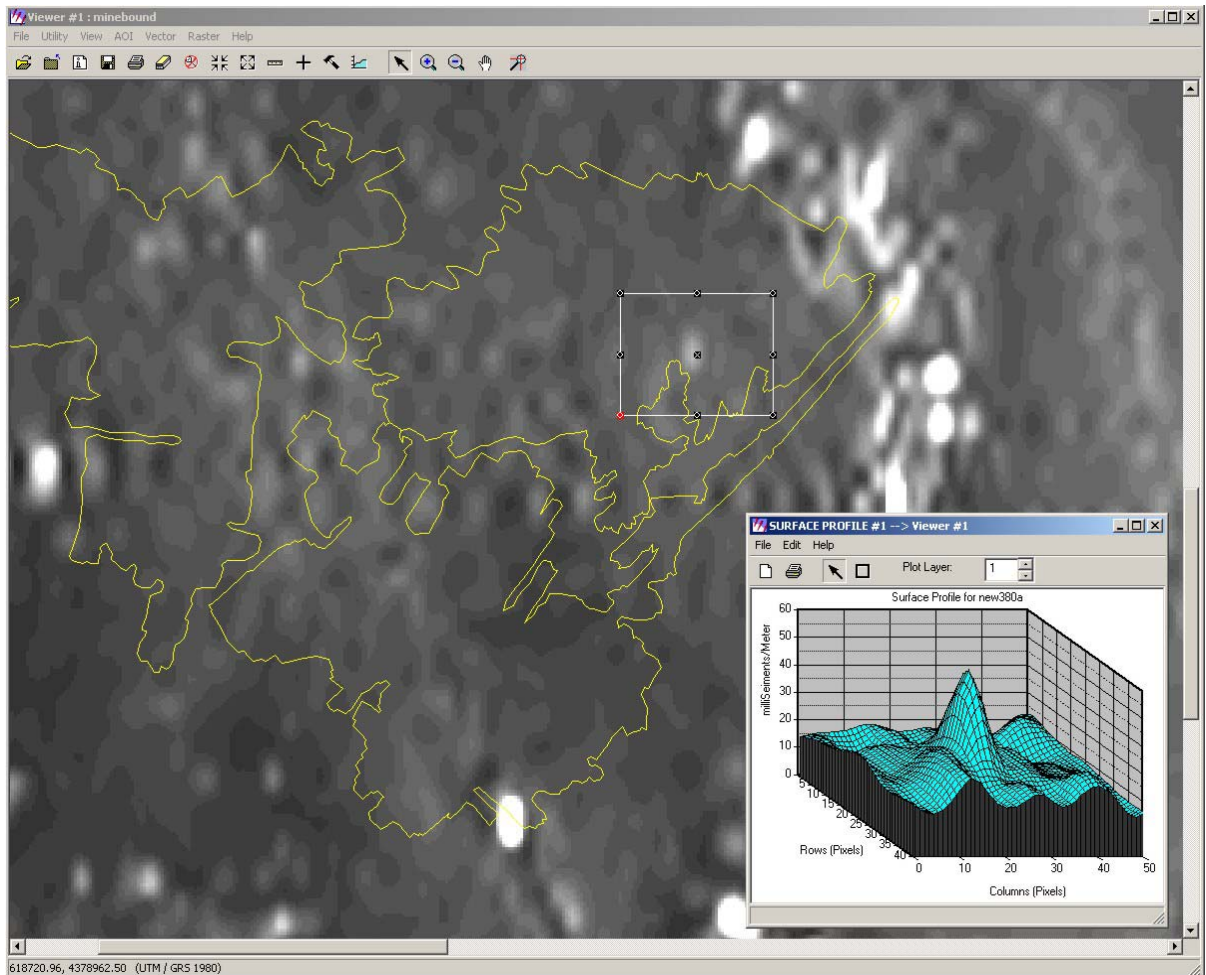

Figure 5.6: The boundary of AMD pool A defined by the 380 Hz frequency data.

The 380 Hz frequency surface profiles shows a very high anomaly that I interpret to represent mine pool A of the AMD at approximately depth 280 feet (Figure 5.6). I do not clearly see similar anomalies for mine pools B and C.

Finally, I just want to mention that the conductivity values increase over the study area where compared with the surrounding areas. The final maps in the Fugro report, they show a loose correlation with topography (Fugro, 2000). For example, in general a topographic high region is often less resistive than a valley. This happens because the valleys have steep topography and as the helicopter flew a traverse over these valleys the distance to the earth increased and lower amplitude values were recorded over this area. This inverse relation between amplitude and altitude results in the signal amplitude being reduced with increasing high or altitude of the sensor (Figure 5.7) (Fugro, 2000).
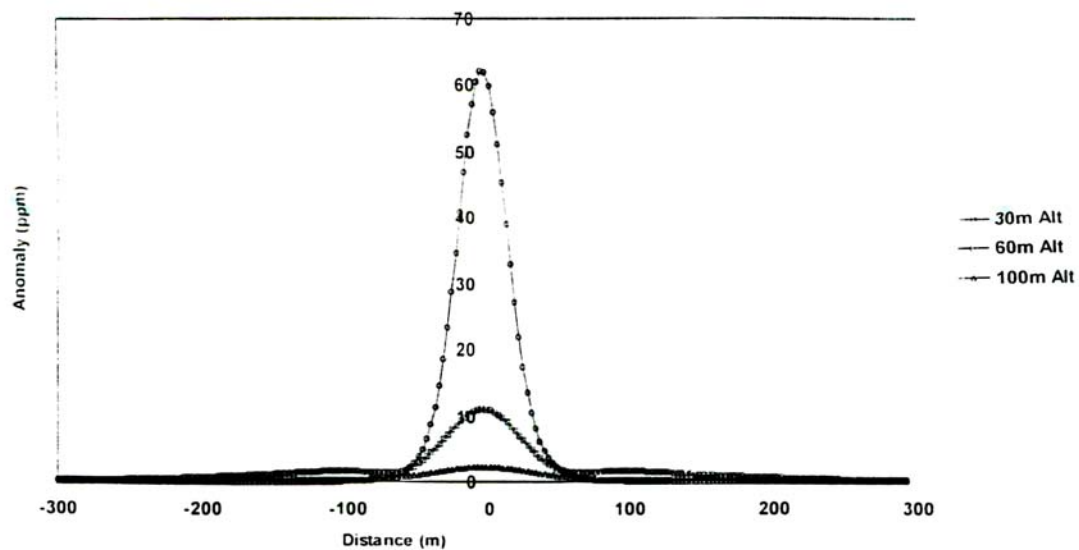

Figure 5.7: The amplitude change over a vertical dike at sensor heights 30 m, 60 m, and 100 m.

Figure (5.8) shows that the topography in our study area and is very gentle. There is

no correlation between conductivity values and the topography in our study area.
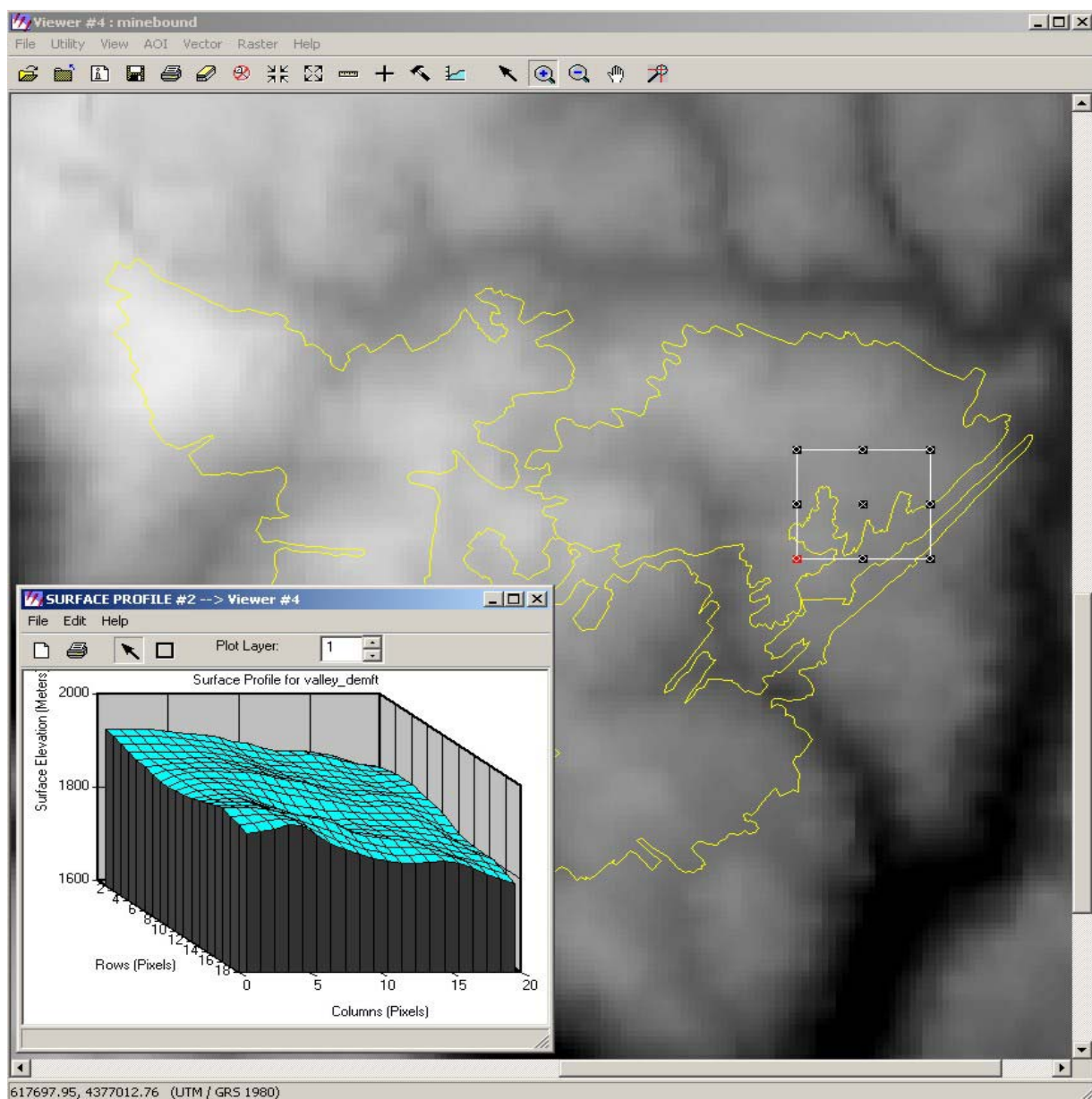
Figure 5.8: The topography in the T&T site, also showing the surface in a 3-D profile.

5.2 Final Results for the Magnetics

The magnetic data in our study area show a smooth regional gradient (Fugro, 2000), from the northwest to the southeast. Figure (5.9) shows the magnetic data over the mine pool A area and a 3-D surface profile show total field magnetic nT. Magnetic results show that relatively non − magnetic rock unit underlies the mine pool A. Figure 5.9 shows a small magnetic anomaly approximately of 5 nT with respect to the surrounding area. I interpret this as related to the subsurface structure. Figure 5.10 shows the magnetic data after I applied high pass filter to remove the degree gradient. After, filtering there are two significant anomalies clearly visible in the mine pool A region and I interpret these as related to subsurface structure possibly the edge of mine pool A.
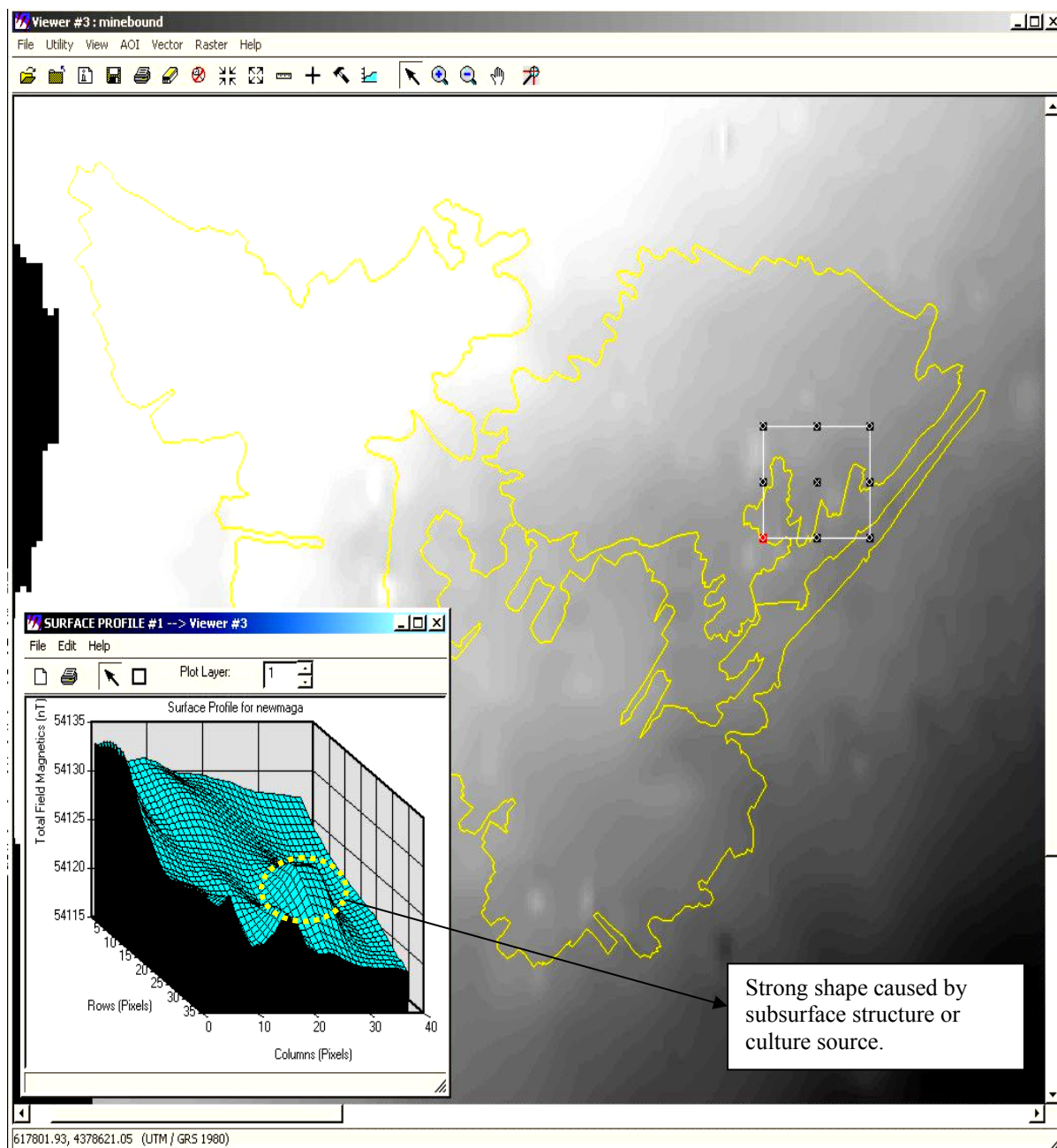
Figure 5.9: Profiles over the mine pool A showing the magnetic data (total field magnetic nT) and a 3-D surface.
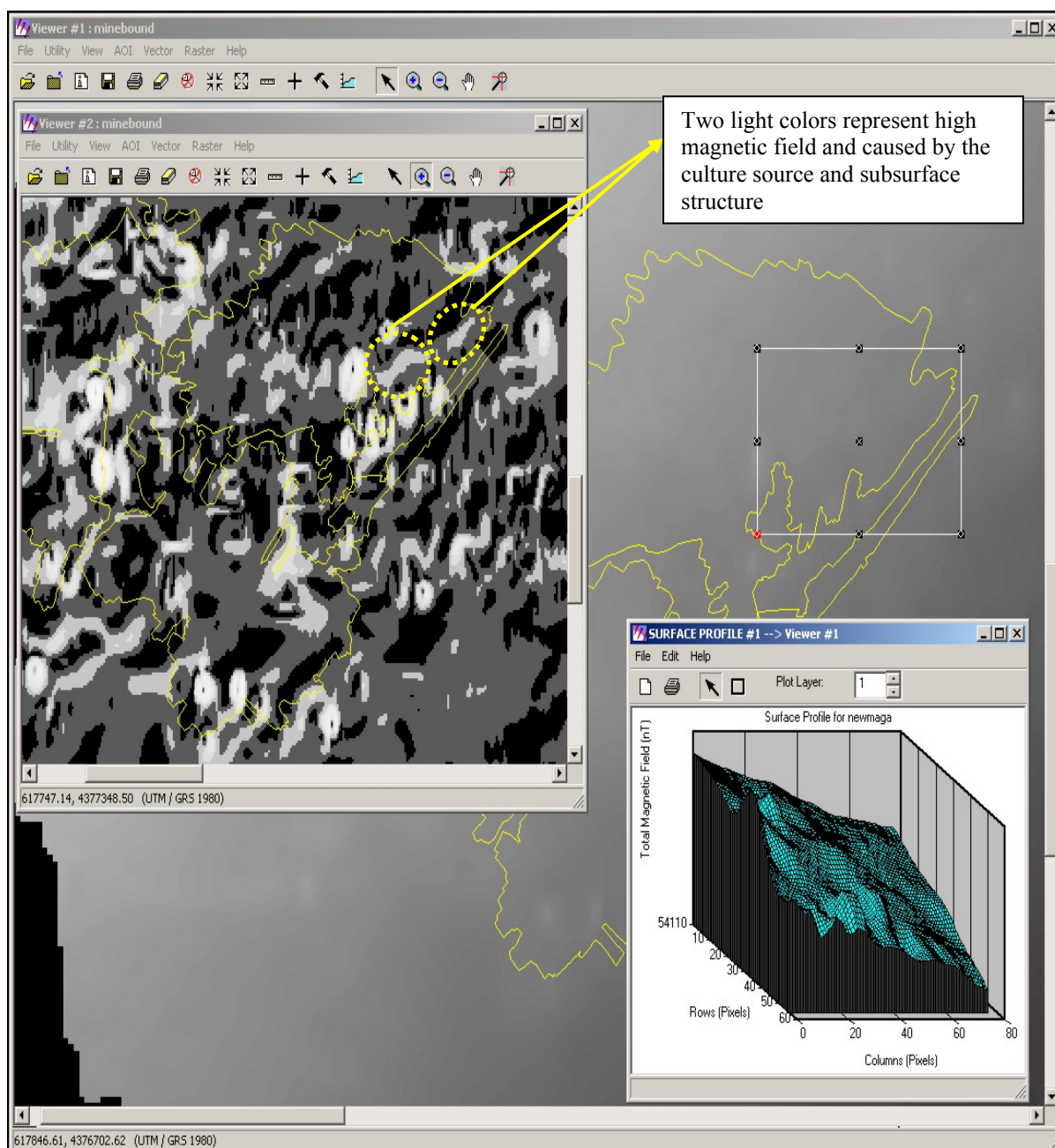
Figure 5.10: High pass filter applied on the raw magnetic data.

5.3 Final Results for the Very Low Frequency VLF

The VLF results showed almost no correlation between data recorded using the transmitting of stations Cutler and Seattle. In addition, there are two gaps in the VLF results for the Muddy and Roaring Creek area. These missing data resulted from the VLF transmitter being turned off during the flight 2 of portions (Seattle station off) and flight 1 (Cutler and Seattle stations off) (Fugro, 2000). Figure (5.11) shows the VLF data of the Cutler station. The Cutler station VLF data around mine pool A dose not show any anomaly.

The Seattle station VLF data (Figure 5.12) shows higher VLF values and one major anomaly. There is not a good correlation between VLF and conductivity results. Overall, I did not obtain any satisfactory results from this method.

Figure 5.11: VLF1 data from the VLF transmitter Cutler station.

Figure 5.12: VLF data of the Seattle station.

6.0 Conclusions

The main goal of this project was to determine the lateral extent of acid mine drainage AMD contaminated mine pools located at a depth of about 300 ft (90m). I believe that there are interpr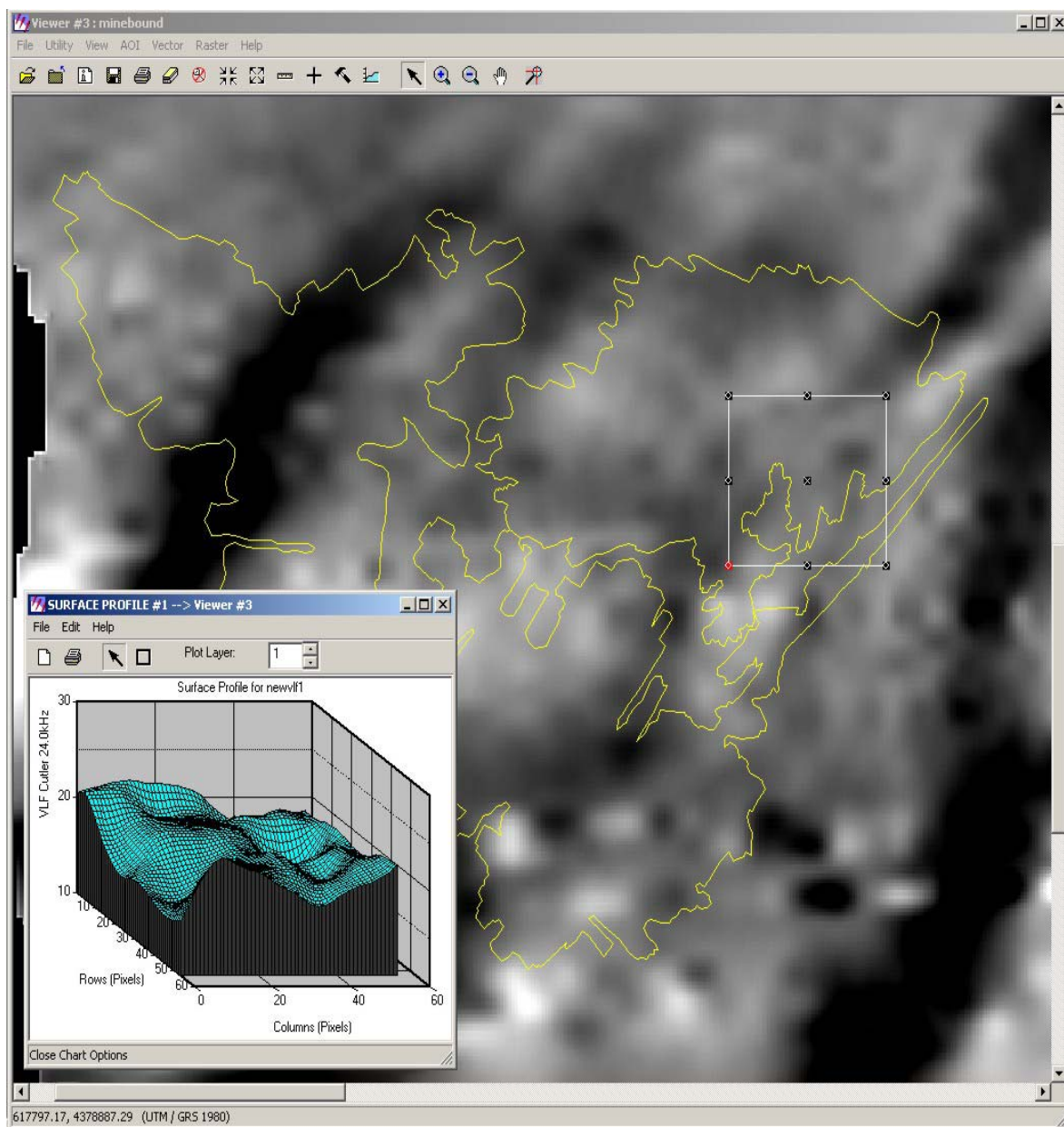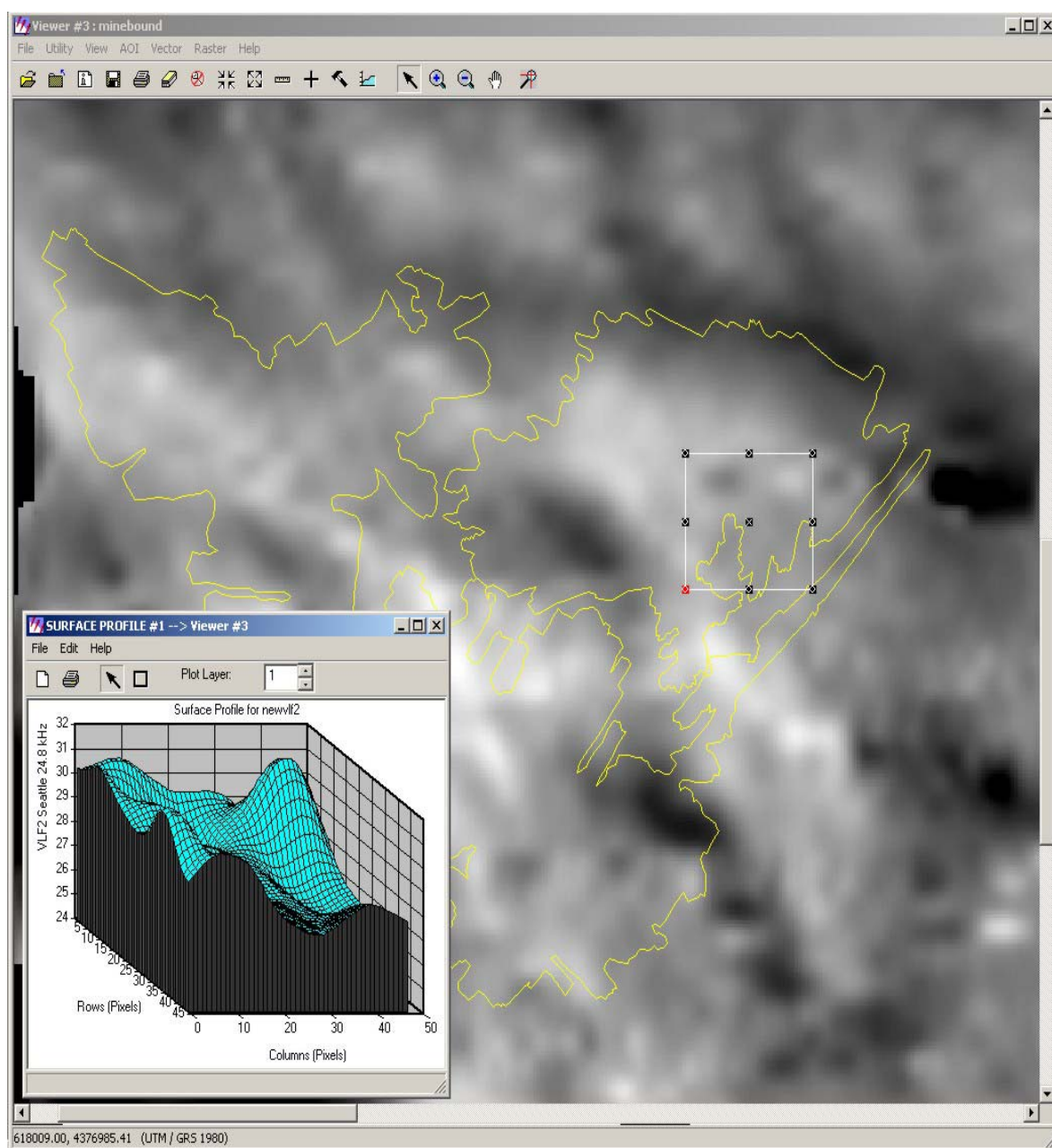etable geophysical proxies for AMD impacted subsurface mine pools. The geophysical data were collected by making an airborne survey using different electromagnetic techniques that included magnetic, conductivity and VLF. Noise was the significant issue in the lowest frequency EM conductivity data, especially the 380 Hz and 1400 Hz data. Common noise sources were power lines, pipelines, and vibration of the EM bird. These noise components were removed from 380 and 1400 Hz. conductivity datasets in ER MAPPER and ERDAS Imagine by applying a variety of spatial frequency filters. ER MAPPER, ERDAS Imagine, ERDAS Virtual GIS, ESRI Arc/Info, and ESRI Arc View software packages were then used to interpret the data. The geometry of the high-conductivity pools were imaged using a variety of techniques including Hue Saturation and Intensity (HSI) algorithms and unsupervised classification. Extraction of cross sections of conductivity was useful to determine the location of anomalies associated with AMD impacted regions. The magnetics data in our study area shows a smooth regional gradient. This smooth gradient display background values grater in the northwest than southeast. Magnetic result shows that relatively non – magnetic rock unit underlies the mine pool A. A small anomaly approximately 5 nT higher than the surrounding area has strong shape noted in mine pool A and I interpret this as related to subsurface structure or may be to cultural sources. The VLF results showed less correlation between of stations Cutler and Seattle. The VLF values in mine pool A from the Cutler station does not show

any anomaly even the light color represent the change in the edges of AMD, I interpret that VLF values are almost similar and close to each other. There is no correlation with similar changes indicated by the conductivity data.

APPENDICIES

Appendix A

Data Collection and Instruments

A.1 Electromagnetic Conductivity

A.1.1 Electromagnetic Conductivity Instrument and the Manufacturer

Electromagnetic System

Model: - DIGHEMvers

Type: - Towed bird symmetric dipole configuration operated at nominal survey altitude of 100 feet. Coil separation is 25.79 feet for all coil pairs (Fugro, 2000).

A.1.2 Type of the Frequency Domain Electromagnetic (FDEM) Conductivity Data Calculated and the Units

The electromagnetic system applied five sets of horizontal coplanar coil-pairs. The result is an in-phase and a quadrature channel from each transmitter-receiver coil-pair. Fugro_Geoterrex Dighem Inc. calculated these conductivities from the following analog-recorded data (Table A.1).

Channel Name Freq.	Parameter	Scale Units/mm
380I	Coplanar in-phase (390 Hz)	5 ppm
380Q	Coplanar quad (390 Hz)	5 ppm
1K4I	Coplanar in-phase (1555 Hz)	5 ppm
1K4Q	Coplanar quad (1555 Hz)	5 ppm
6K2I	Coplanar in-phase (6254 Hz)	10 ppm
6K2Q	Coplanar quad (6254 Hz)	10 ppm
25KI	Coplanar in-phase (25,800 Hz)	20 ppm
25KQ	Coplanar quad (25,800 Hz)	20 ppm
102I	Coplanar in-phase (102,680 Hz)	20 ppm
102Q	Coplanar quad (102,680 Hz)	20 ppm

Table A.1: The Frequency Domain Electromagnetic (FDEM) Conductivity Analog Profiles (Fugro, 2000).

The apparent conductivity can be existed in milliSiemens/meter (mS/m) from the in-phase and quadrature EM components of any frequencies (Table 8.2).

Channel	Computed Parameters	Scale Units/mm
CON 380	Log Conductivity (milliSiemens /meter)	.04 decade
CON 1400	Log Conductivity (milliSiemens /meter)	.04 decade
CON 6200	Log Conductivity (milliSiemens /meter)	.04 decade
CON 25000	Log Conductivity (milliSiemens /meter)	.04 decade
CON 102000	Log Conductivity (milliSiemens /meter)	.04 decade

Table A.2:   This table shows the Computed parameters (Fugro, 2000).

The log conductivity (millisemens/meter)   .04 decade means that the conductivity changes by an order of magnitude in 25 mm. The conductivity at 0, 25 and 50 mm up from the bottom of the digital profile are respectively 0.1, 1.0 and 10 ms/m.

Apparent conductivity maps, which display the conductive properties of the survey areas, were produced from the 390 Hz, 1555 Hz, 6254 Hz 25.800 Hz and 102.680 Hz coplanar Data.

A.2 Magnetic

A.2.1 Magnetic Instrument and the Manufacturer

Model: - Picodas 3340 processor with Geometrics G822   sensor

Sensitivity: - 0.01 nT

The magnetometer sensor is housed in separate bird. 70 ft (21m) below the

Helicopter.

A.2.2 Magnetic Base Stations

Model: - GEM System GSM –19T

Model: - Picodas MEP–710 processor with Geometric G823 Sensor

A.2.3 Type of the Magnetic Data calculated and the Units

Channel Name Freq.	Parameter	Scale Units/mm	On the Digital Profile
MAGF	Magnetic (fine)	2.0 nT	MAG1
MAGC	Magnetic (coarse)	20 nT	MAG25

Table A.3: The Analog profiles show the magnetic calculated data.

The all magnetic field data presented as contours on the base maps using a contour inter-

val of 2 nT. The field survey shows the magnetic properties of the rock units underlying

the survey areas or magnetic properties of the earth materials in the survey area. The in-

formation can be used to locate magnetic bodies of direct interest for exploration and for

structure and lithological mapping.

A.3 Very Low Frequency (VLF-EM)

A.3.1 Name of the Instrument and the Manufacturer VLF System

Manufacture: - Herz Industries Ltd.

Type: - Totem –2A

Station: - Seattle NLK   24.8 K Hz

- Cutler NAA   24.0 K Hz

The VLF sensor is housed in a separate bird that is towed 32 ft below the helicopter.

A.3.2 Type of the VLF-EM Data calculated and the Units

Channel Name Freq.	Parameter	Scale Units/mm	On the Digital Profile
VF1T	VLF-total: Cutler (24.0)	2%	VLFT1
VF1Q	VLF-quad: Cutler (24.0)	2%	VLFQ1
VF2T	VLF-total: Seattle (24.8)	2%	VLFT2
VF2Q	VLF-quad: Seattle (24.8)	2%	VLFQ2

Table A.4: the analog profiles of the VLF calculated data by Fugro.

The VLF receiver measures the total field and vertical quadrature components of the secondary VLF field.   The VLF results are obtained from two transmitting stations (Seattle NLK   and   Cutler NAA). The VLF snaps show the contoured results of the total field from each respective station (Fugro, 2000).

Appendixes B

Data Dictionary

ALGORITHM	CLASSIFICATION CLASSES	OUTPUT IMAGE
Classes.alg	10 Classes Established	Classification_01.tiff
Classes_255.alg	255 classes Established	Classification_02.tiff

Table B.1: Unsupervised Classification Images

ALGORITHM	CHANNEL1	CHANNEL2	CHANNEL3	TRANSFORM	COMMENT	OUTPUT IMAGE
HSI _1. alg	Hue = 25K_Raw.ers	Saturation = 6200_Raw_1.ers	Intensity= 380Raw_Noise3.ers	Histogram Equalize H S and I	Pool boundaries are well expressed	H S I 1 Algorithm IMAGE_01.TIFF
HSI _2. alg	Hue = 6200_Raw_1.ers	Saturation = VLF1T_Raw.ers	Intensity= 102k_Raw1.ers	Histogram Equalize H S and I	Pool boundaries are well expressed	H S I 1 Algorithm IMAGE_02.TIFF
HSI _3. alg	Hue = 102k_Raw.ers	Saturation = 6200_Raw_1.ers	Intensity= Mag.ers	Histogram Equalize H S and I	Pool boundaries are well expressed	H S I 1 Algorithm IMAGE_03.TIFF
HSI _4. alg	Hue = 25K_Raw.ers	Saturation = 1400Raw_Noise.ers	Intensity= VLF1T_Raw.ers	Histogram Equalize H S and I	Pool boundaries are well expressed	H S I 1 Algorithm IMAGE_04.TIFF
HSI _5. alg	Hue = 102k_Raw1.ers	Saturation = 1400Raw_Noise.ers	Intensity= 25k_Raw.ers	Histogram Equalize H S and I	Pool boundaries are well expressed	H S I 1 Algorithm IMAGE_05.TIFF
HSI _6. alg	Hue = VLF1T.ers	Saturation = 1400Raw_Noise.ers	Intensity= 25k_Raw.ers	Histogram Equalize H S and I	Pool boundaries are well expressed	H S I 1 Algorithm IMAGE_06.TIFF
HSI _7. alg	Hue = 6200_Raw.ers	Saturation = VLF1T.ers	Intensity= Mag.ers	Histogram Equalize H S and I	Pool boundaries are well expressed	H S I 1 Algorithm IMAGE_07.TIFF
HSI _8. alg	Hue = 25K_Raw1.ers	Saturation = 1400_noise.ers	Intensity= 6200_Raw_1.ers	Histogram Equalize H S and I	Pool boundaries are well expressed	H S I 1 Algorithm IMAGE_08.TIFF

Table B.2: Hue Saturation and Intensity Images

BIBLIOGRAPHY

Bibliography

Ackman, T.E., G.A. Veloski, R.A. Dotson, Jr., R.W. Hammack, J.I. Sams, 2000. An Evaluation of Remote Sensing Technologies for Watershed Assessment. U.S. Department of Energy, National Energy technology Laboratory, Pittsburgh, PA.

Blakely, R.J., 1995, *Potential theory in gravity and magnetic applications* (Standard Cambridge Program). New York: Cambridge University Press. 441 p.

Brian, C. M., Ground Based Magnetometer survey of Abandoned wells at the Rocky Mountain Arsenal – A Case History: Geragth & Miller, Inc.

Dobrin, M.B., and Savit, C.H., 1988, *Introduction to geophysical prospecting 4th edition*: McGraw-Hill, Inc., New York. 630 p.

ER MAPPER User Guide 6.0, 1998: Earth Resource Mapping Pty Ltd. 922 p.

ERDAS Imagine Virtual GIS V8.4, 1997, ERDAS, Inc. 656 p.

Evangelou, V. P., 1995. *Pyrite oxidation and its control*. Boca Raton, FL: CRC Press, 293 p.

Fitterman, D. V., and Deszcz-Pan, M. 1998, Helicopter EM mapping of saltwater intrusion in Everglades National Park, Florida, Exploration Geophysics., 29, 240-243.

Fugro_Geoterrex Dighem, Inc., 2000. Report for US Dept. of Energy.

Gilkeson, R.H., Heigold, P. C., and Laymon, D.E., 1986, Practical Application of theoretical models to magnetometer surveys on hazardous waste disposal sites- a case history and Technology Center over the Cheat River Watershed, #996004.

Hennin, R.V., and Reger, D.B., 1914, Preston County: West Virginia Geological and Economic Survey County Report, 566 p.

Hobba, W.A., 1991. Relation of fracture systems to transmissivity of coal and overburden aquifers in Preston County, West Virginia: USGS Water-resources Investigation Report 89-4137.

Interpretation of Magnetic Data Available:
http://www.gcn.ou.edu/~jahern/g&m/mag_interp/mag_interp.html

Kaikkonen, P., 1997. Some points of view concerning interpretation of VLF and VLF-R measurements: University of Miskolc, Series A Mining, Vol. 52 No. 1, pp.81-101

Keary, P., Brooks, M. 1991. *An Introduction to Geophysical Exploration 2ⁿᵈ edition*: Blackwell Scientific Publications, Boston. 254 p.

Keller, G.V. and Frank C. Frischknecht, Electrical Methods in Geophysical Prospecting, International Series of Monographs in Electromagnetic Waves, Volume 10, Pergamon Press, 1926.

Kimmel, W.G., 1983, The impact of acid mine drainage on the stream ecosystem, in Majumdar, S.K., and Miller, W.W., eds., Pennsylvania Coal: Resources, Technology, and Utilization, The Pennsylvania Academy of Science Publishers, 424-437 p.

Kleinmann, R.L.P., 1989, Acid mine drainage: U.S. Bureau of Mines researches and develops control methods for both coal and metal mines: Eng. Min. J., v. 190, p.16I-16N.

McNeill, J.D., 1980, Electromagnetic Terrain Conductivity Measurements at Low Induction Numbers: Mississauga, Ontario, Canada, Geonics Ltd. Technical Note TN-6, 15 p.

McNeill, J.D., 1986, Geonics EM39 borehole conductivity meter. Theory of Operation: Geonics Technical Note TN-20.

McNeill, J.D., 1990. Use of electromagnetic methods for groundwater studies: Geotechnical and Environmental Geophysics, v. 1, 191-217 pp.

Meehan, G.M., 1980, Geologic factors affecting the mining of the upper Freeport coal seam in west central Preston County, West Virginia: Pittsburgh, PA, MS Thesis, University of Pittsburgh.

Office of Surface Mining, www.osmre.gov/amdform.htm: Washington, D.C. 07/16/2002 21:13:55

Owens, R.,10/29/1997, Computer Vision IT412, Department of Computer Science

http://www.dai.ed.ac.uk/CVonline/LOCAL_COPIES/OWENS/LECT5/node4.htm

l#SECTION00040000000000000000

Paterson, N.R., and Ronka, V., 1971, Five years of surveying with the very low frequency electro method. Geoexploration, v.9, 7-26 p.

Reynolds, J.M., 1997. *An Introduction to applied and environmental geophysics*: John Wiley & Sons Ltd, Baffins Lane, Chichester, West Sussex PO19 1UD, England. 796 p.

Rose, A. W., Cravotta, C. A., III, 1998, Geochemistry of coal mine drainage, in Brady K.B.C., Smith, M.W., and Schueck, J., eds., Coal Mine Drainage Prediction and Pollution Prevention in Pennsylvania: Harrisburg, Department of Environmental Protection, 1-1 to 1-22 p.

Sander Geophysics Limited, Interpretation of Airborne Geophysical Data: http://www.sgl.com/services/interpr.html

Sharma, P. V., 1997. *Environmental and Engineering Geophysics*: Cambridge University Press, New York. 475 p.

Stafford, S.L., 1999, Strontium-Isotopic ratios trace natural alkaline addition to coal mine drainage: Pittsburgh, PA, University of Pittsburgh.

Stewart, M.T., 1981. Evaluation of electromagnetic terrain conductivity measurements for detection and mapping of salt water interfaces in coastal aquifers: Florida water resources research center.

Telford, W.M., Geldart, L.P., Sheriff, R.E., 1990, *Applied Geophysics 2nd* : Cambridge University Press, New York. 770 p.

Valleau, N. C., March 2000, HEM Data Processing – A Practical Overview: 14th ASEG Conference & Exhibition, Perth.